DLK-dependent mitochondrial fission drives axon degeneration and neuronal cell death

Jorge Gómez-Deza J [1], Matthew Nebiyou[1], Mor R. Alkaslasi[1], Preethi Somasundaran[2], Anastasia L. Slavutsky[1], Michael E. Ward[3], Trent A. Watkins[2], Claire E. Le Pichon[1]

[1] *Eunice Kennedy Shriver* National Institute of Child Health and Human Development, National Institutes of Health, Bethesda, United States
[2] Departments of Neurosurgery and Neuroscience, Baylor College of Medicine, Houston, Texas
[3] National Institute of Neurological Disorders and Stroke, National Institutes of Health, Bethesda, United States

Abstract

Currently there are no effective treatments for an array of neurodegenerative disorders to a large part because cell-based models fail to recapitulate disease. Here we developed a robust human iPSCbased model where laser axotomy causes retrograde axon degeneration leading to neuronal cell death. Time-lapse confocal imaging revealed that damage triggers a wave of mitochondrial fission proceeding from the site of injury to the soma. We demonstrated that mitochondrial fission and resultant cell death is entirely dependent on phosphorylation of dynamin related protein 1 (DRP1) by dual leucine zipper kinase (DLK). Importantly, we show that CRISPR mediated *Drp1* depletion protected mouse retinal ganglion neurons from mitochondrial fission and degeneration after optic nerve crush. Our results provide a powerful platform for studying degeneration of human neurons, pinpoint key early events in damage related neural death and new focus for therapeutic intervention.

Introduction

Neuronal death and axon loss are universal hallmarks of neurodegeneration, relevant to Alzheimer's disease, ALS and other neurodegenerative diseases. However, our understanding of the mechanisms controlling axon degeneration and neuron death is incomplete. Advances in this area have enormous potential to benefit all types of neurodegenerative conditions including those arising from nerve injury and traumatic brain injury.

Separate mechanisms regulate axon degeneration and neuronal apoptosis[1]. For example, deletion of BAX (BCL-2-associated X protein), a central regulator of apoptosis, does not protect axons from Wallerian degeneration. On the other hand, BAX deletion protects neurons following trophic factor withdrawal, a developmental model of axon degeneration and death[2]. SARM1 is the central executioner of Wallerian axon degeneration[3,4]. However, it is unclear how universal this pathway is for axon degeneration since some neurodegenerative models are not rescued by loss of SARM1[5,6]. Furthermore, while most neurodegenerative diseases involve loss of axons and cell bodies, Wallerian axon degeneration does not regulate neuronal cell death.

Mitochondria are a central hub of axon health regulation, at the nexus of axonal energy production, oxidative stress, and calcium buffering[7,8]. They also play critical roles in degeneration and regeneration[9,10]. Healthy maintenance of the mitochondrial network is mediated by a balance of mitochondrial fission and fusion regulated by specialized machinery[11]. Interestingly, mutations in some of these genes cause neurodegenerative conditions such as motor and sensory neuropathy (eg. Mfn1 in Charcot-Marie-Tooth[12]). A key player in the mitochondrial fission process is dynamin related protein 1 or DRP1, a GTPase that oligomerizes around the outer mitochondrial membrane to cause mitochondrial fission[13]. DRP1 also regulates apoptotis[11,14–16]. Under conditions that drive apoptosis, DRP1 promotes a type of apoptotic mitochondrial fission in which BAX permeabilizes the outer mitochondrial membrane, allowing the release of pro-apoptotic factors such as cytochrome c[17,18].

Much of what we know about mechanisms regulating neuron degeneration and death comes from a wealth of studies of apoptosis in cell lines (but not neurons), or from animal models (neurons, but not human). How translatable this work is and how applicable to neurons remains to be determined. One well established model of retrograde axon degeneration is a trophic factor deprivation model, in which embryonic mouse primary neurons are deprived of NGF (nerve growth factor), which leads to their degeneration[19,20]. Recent advances in iPSC-derived neuron techniques now enable the generation of a diverse range of human neuron subtypes. These efforts have already generated exciting findings in the neurodegeneration field[21–23]. We therefore set out to study axon injury using a widely-adopted glutamatergic neuron model (i3Neurons[24]).

We and others have shown that the dual leucine zipper kinase (DLK, or MAP3K12), is a key regulator of axon degeneration and a driver of neuron cell death[25–29]. The canonical DLK pathway involves a phosphorylation cascade downstream of DLK homodimerization and a transcriptional

stress response, including phosphorylation of the transcription factor cJun[29]. Despite its consideration as a drug target for several neurological conditions, relatively little is known about DLK function in human neurons.

Here, we investigate the behavior of i3Neurons following laser axotomy, and the role of DLK in the injury response of human neurons. Following axotomy, we observe progressive retrograde axon degeneration from the injury site back towards the cell body, causing subsequent neuronal death, establishing a unique human model of neurodegeneration. This contrasts with the behavior of cultured mouse neurons, which survive and regenerate after this type of injury[30–32], but resembles the pattern of neurodegeneration observed in optic nerve injuries in living mice[26].

In axons proximal to the injury, mitochondria shrink and undergo DRP1-dependent fission in a retrograde wave, leading to apoptosis of the cell body. DLK regulates mitochondrial fission via direct phosphorylation of DRP1 at serine 616. Such DRP1 phosphorylation by DLK is necessary for localization of BAX to axonal mitochondria, which causes axon degeneration. Blocking DLK or DRP1 protects axons from degeneration and neurons from cell death both in human i3Neurons *in vitro* and *in vivo* in the mouse. This interaction between DLK and DRP1 identifies a new substrate for DLK, a new kinase for DRP1, and a novel signaling pathway for DLK. Collectively, our findings reveal an apoptotic cascade that is initiated in the axon that both underlies non-Wallerian axon degeneration and drives neuronal cell death.

Results

Axotomy in human neurons causes both proximal and distal axon degeneration

Axotomy has often been used as a method to study axon degeneration. After axotomy, the distal portion of the axon undergoes Wallerian degeneration, a phenomenon controlled by the NADase SARM1, the key executioner of this type of axon degeneration[3,4]. To study the response of human neurons to axotomy, we performed laser axotomies in i3Neurons that were sparsely transduced with a fluorescent protein to visualize individual neurons (Fig. 1A). The distal portion of these axons underwent Wallerian degeneration as expected (Fig. 1B, C). To our surprise, we observed that the portion of the axon proximal to the injury and still connected to the cell body underwent progressive retrograde axon degeneration (Fig. 1B-C). Because SARM1-dependent degeneration relies on the loss of the axon survival factor NMNAT2, which occurs when the axon is severed from the cell body, we hypothesized that the proximal axon degeneration we observed might not rely on SARM1 and might provide an opportunity to elucidate novel pathways of axon degeneration.

We tested the requirement for SARM1 in the degeneration of axons both proximal and distal to the injury site. Using CRISPR/Cas9, we knocked out SARM1 in i3Neurons [33]. We then axotomized these neurons and control neurons and imaged the axon on both sides of the injury. As expected, SARM1 was necessary for distal axon degeneration, but not proximal axon degeneration (Fig. 1B-C). We therefore decided to investigate the mechanisms underlying proximal axon degeneration in these neurons. For the remainder of the study, we focus specifically on the axon segment proximal to the injury site.

Axotomy in human neurons triggers a wave of DRP1-dependent mitochondrial fission

Mitochondria play pivotal roles in axon degeneration, due to their importance in energy production, calcium homeostasis, production of reactive oxygen species and signaling[34,35]. We transduced i3Neurons with a mitochondrial-targeted GFP and plated them in the center of wells to allow axons to project outwards and visualize individual axons. After axotomy, mitochondria underwent rapid shrinkage (Fig. 1D-G; Video S1) and increased in number (Fig. 1H). Using live imaging, we determined that the increase in mitochondrial number was due to fission events rather than mitochondrial transport and localization to the site of injury. Mitochondrial fission was most evident from close analysis of live imaging (Video S1 and Fig. 1D-E).

Mitochondrial fission is a dynamic process that is regulated by proteins localized in the inner and outer mitochondrial membranes[13]. A critical regulator of fission is dynamin related protein 1 (DRP1), a cytoplasmic GTPase. DRP1 is recruited to the outer mitochondrial membrane and helically oligomerizes around the mitochondrion to constrict it and bring about scission of the membrane. To test whether the fission we observed was dependent on DRP1, we knocked down DRP1 using CRISPR interference by expressing a previously validated guide RNA to DRP1 in i3Neurons expressing a catalytically dead Cas9 (dCAS9)[21,33]. DRP1 knockdown prevented the increase in mitochondrial particle number (Fig. 1H). We confirmed this result by inhibiting DRP1 using P110, a peptide that blocks the interaction between DRP1 and FIS1 (mitochondrial fission

135 protein 1), another protein that is essential for fission (Fig. 1I). In line with previous reports[36,37],
136 these events were dependent on calcium influx into the injured axon which, when buffered using
137 BAPTA-AM, also prevented mitochondrial fission (Fig. S1A-D; Videos S2-5).
138
139
140 **Mitochondrial fission precedes proximal axon degeneration**
141 To characterize the spatial and temporal dynamics of the axonal response to injury, we analyzed
142 mitochondrial fission and axon degeneration in 100 µm segments of the axon relative to the
143 injury site every 10 min following axotomy. This analysis revealed that mitochondrial fission
144 began seconds after injury and progressed in a retrograde manner back towards the cell body.
145 One hour after axotomy, mitochondria 500 µm away from the injury had undergone fission (Fig.
146 1J-K Video S6). This fission preceded a slower retrograde wave of axon degeneration back
147 towards the cell body (Fig. 1L-M, Video S7).
148
149 Time lapse imaging of the cell bodies of axotomized neurons revealed that the retrograde wave
150 of axon degeneration was followed by fragmentation of mitochondria in the soma and cell death
151 (Fig. 1N-O; Videos S8-9). Axotomy led to death of 84% of cells analyzed. We have thus uncovered
152 an exciting new human neuron model in which axon injury initiates progressive dying back of the
153 axon and ultimately results in neuronal cell death.
154
155
156 **DLK regulates axotomy-induced mitochondrial fission**
157 To understand mechanisms governing neurodegeneration in this model, we started by examining
158 a pathway involved in the cellular response to axon injury. The dual leucine zipper kinase (DLK;
159 MAP3K12) is a key regulator of the axon damage response and neuronal cell death [29,38]. Because
160 mitochondria are critical regulators of axon degeneration, we were curious whether DLK protein
161 might localize to axonal mitochondria. In i3Neurons, we observed association of DLK with 77% of
162 axonal mitochondria (Fig S2 A-C). We further corroborated this association by immuno-EM (Fig.
163 S2D), and through observation of DLK co-trafficking with mitochondria (Fig. S2E).
164
165 To investigate how DLK responds to axon damage in human neurons, we performed laser
166 axotomies and live imaging of DLK and mitochondria. We observed an intriguing presence of DLK
167 puncta at 45% of sites of mitochondrial fission (Fig. 2A-B, Video S10). To determine whether DLK
168 influences mitochondrial fission, we generated DLK KO neurons using CRISPR/Cas9 (Fig. S2F). The
169 knockout neurons were validated by immunofluorescent staining and western blotting (Fig. S2G-
170 H). In the absence of injury, we observed no mitochondrial phenotypes in these cells including
171 number, size, movement, and oxygen consumption rate (Fig. S2I-P). Strikingly, DLK KO neurons
172 did not exhibit the axonal mitochondrial fission we had observed in response to axotomy in wild
173 type neurons (Fig. 2C-D; Videos S11-12). Corroborating this result, pharmacological inhibition of
174 DLK using GNE3511 prevented mitochondrial fission after injury (Fig. 2E, Videos S13-14).
175
176 To better understand the mechanism by which DLK regulates mitochondrial fission, DLK KO
177 neurons were transduced with wild type DLK or 2 mutant versions of DLK. DLK C127S cannot be
178 palmitoylated, hindering its ability to properly signal[39] . Kinase dead DLK (S302A) cannot be trans-

179 phosphorylated and is catalytically inactive [27,40]. Only the expression of wild type DLK rescued the
180 fission phenotype in DLK KO neurons (Fig. 2F; Videos S15-17), indicating that DLK kinase activity
181 is critical for this process. We thus uncover a role for DLK in regulating mitochondrial fission after
182 injury.
183
184
185 **DLK directly phosphorylates DRP1 to induce mitochondrial fission**
186 DRP1 phosphorylation state regulates its function state, with phosphorylation at serine 616
187 promoting mitochondrial fission[41]. We speculated that DLK might phosphorylate DRP1 at this
188 residue. In order to more easily study this signaling mechanism, we turned to a heterologous
189 system, HEK293 cells, that do not express DLK. Overexpression of DLK in these cells can be used
190 to study DLK signaling since its homodimerization is sufficient to drive pathway activity [40,42].
191
192 Expression of wild type DLK, but not DLK C127S (palmitoyl-site mutant) or DLK S302A (kinase
193 dead), resulted in DLK signaling as reflected by the increased phosphorylation of its downstream
194 target c-Jun (Fig. 3 A-B). Interestingly, when we co-expressed DLK and DRP1, phosphorylation at
195 S616 was increased in this model of DLK activation (Fig. 3 A, C), but not with mutant DLK, showing
196 that DLK activity is sufficient to cause DRP1 S616 phosphorylation. Levels of total DRP1 remained
197 unchanged, as did levels of S637 pDRP1, a site whose phosphorylation is thought to impair DRP1
198 GTPase activity [43,44] (Fig. 3 A, D-E).
199
200 To further validate that DLK signaling causes DRP1 phosphorylation, we purified GST-DRP1 from
201 HEK293 cells expressing wild type DLK or DLK S302A, and performed targeted mass spectrometry
202 to quantify DRP1 phosphorylation (Fig. 3F). The relative abundance of phospho-DRP1 S616
203 peptides was significantly increased only in the HEK293 cells expressing wild type but not kinase
204 dead DLK (Fig. 3G). These results demonstrate that DLK kinase activity can promote DRP1
205 phosphorylation at S616 either directly or indirectly.
206
207 Next, to determine whether DLK can directly phosphorylate DRP1, we performed an *in vitro*
208 kinase assay using proteins separately purified from HEK293 cells. Remarkably, incubation of
209 DRP1 with wild type DLK increased pDRP1 S616, whereas incubation with kinase dead DLK did
210 not (Fig. 3H,I). We thus demonstrate that DLK can directly phosphorylate DRP1 at serine 616.
211
212 To link this phosphorylation of DRP1 to a potential effect on mitochondria, we analyzed
213 mitochondrial morphology in the HEK293 cells. Similar to what we had observed in injured axons,
214 DLK signaling resulted in an increase in mitochondrial fragmentation (Fig. 3 J,K). DLK-induced
215 mitochondrial fragmentation was prevented by knocking down DRP1 (Fig. 3 K-N). These data
216 identify DLK as a novel kinase of DRP1 whose role is to drive mitochondrial fission via direct
217 phosphorylation of DRP1 at serine 616.
218
219
220 **Axotomy causes DLK-dependent phosphorylation of DRP1**
221 To validate these results in the i3Neurons, DLK KO or WT neurons were center-plated such that
222 axon fractions could be harvested to examine axonal DRP1 phosphorylation after injury (Fig. 4A).

223 Two hours after axotomy, phospho-DRP1 S616 (pDRP1 S616) was increased in axons but not cell
224 bodies of wild type neurons. This did not occur in DLK KO neurons (Fig. 4B-E). The increase in
225 pDRP1 S616 in wild type but not DLK KO axons was further validated by immunostaining (Fig. 4F-
226 G).
227
228 To examine whether DRP1 phosphorylation at S616 also occurs *in vivo*, we performed optic nerve
229 crush in mice. Increased pDRP1 S616 relative to total DRP1 was detected in optic nerve proximal
230 to the crush site 24 hours after injury (Fig. 4H-J). Levels of total DRP1 in injured nerves remained
231 unchanged (Fig. 4I,K). We next asked whether DLK also regulates the phosphorylation of DRP1 *in*
232 *vivo* after injury. Optic nerve crush was performed in mice treated with vehicle or DLK inhibitor
233 GNE-3511. We observed a reduction in the levels of pDRP1 S616 relative to total DRP1 in mice
234 treated with GNE-3511 compared to the vehicle controls, demonstrating that axon injury triggers
235 DLK-dependent DRP1 phosphorylation *in vivo* as well as *in vitro.*
236
237
238 **Inhibiting DRP1 delays axon degeneration and neuron death**
239 Since axotomy leads to progressive degeneration of the axon proximal to the injury and
240 eventually to cell death, we asked to what extent DLK and DRP1 control the degeneration of each
241 compartment. DLK has been shown to contribute to axon degeneration and to neuron death in
242 many contexts [25–29,45]. We hypothesized that DLK would promote axon degeneration in
243 axotomized human neurons. Whereas wild type axons had degenerated as early as 4 hours after
244 injury, DLK KO axons were still present after 24 hours (Fig. 5A-C). Interestingly, in neurons with
245 CRISPRi knockdown of DRP1, axons were also protected from degeneration (Fig. 5D-F).
246
247 To determine whether loss of DLK or DRP1 also protected neurons from death, we followed the
248 fate of cell bodies of axotomized neurons. In control neurons we observed cell death in about
249 70% of cells after axotomy whereas only 18% of DLK KO cells and 33% of DRP1 knockdown cells
250 died (Fig 5G-L). These results demonstrate that DRP1 and DLK are key regulators of neuronal cell
251 death after axotomy.
252
253
254 **Loss of DRP1 prevents neuron death after axotomy *in vivo***
255 We then asked how universal this pathway is, or whether it was unique to the i3Neuron model.
256 It has been established that silencing DLK blocks retinal ganglion cell (RGC) death after optic nerve
257 crush [26,27,45,46]. However, DRP1 has not previously been implicated downstream of this DLK
258 signaling. To knock down DRP1, we used an AAV delivery strategy to express a small Cas9 (sa-
259 Cas9) together with a guide RNA to DRP1 [47]. AAVs were injected into the intravitreal space to
260 transduce RGCs. Optic nerve crush was performed two weeks later, and retinas were harvested
261 3 days post injury, a time point at which injured RGCs express cleaved caspase 3 (Fig. 5M). The
262 average number of cleaved caspase 3-positive RGCs with saCas9 and a control gRNA was similar
263 to a control virus expressing just EGFP (55 $\pm$ 7.83 and 61 $\pm$ 6.24, respectively (Fig 5O). However,
264 knocking down DRP1 significantly reduced the caspase positive cell count to 20 $\pm$ 8.93 (Fig. 5N-
265 P), demonstrating that this DRP1-dependent pathway is essential for neuronal cell death after
266 axon injury *in vivo*.

267
268
269 **BAX mediates cell death after axotomy**
270 To better understand this type of axon degeneration and cell death, we asked whether they
271 occurred via canonical pathways of apoptosis, and in particular whether they involved BAX. In
272 models of apoptosis, DRP1 contributes to BAX recruitment to mitochondria [48], and DRP1 and BAX
273 interact to drive mitochondrial depolarization and fragmentation [18,49]. Jenner et al. showed a
274 close interaction between DRP1 and BAX in HEK cells undergoing apoptosis using a fluorescence
275 complementation biosensor (ddRFP [50]). This system produces enhanced red fluorescence upon
276 dimerization of A_1 and B_1 proteins. Using A_1-DRP1 and B_1-BAX fusion constructs, we tested
277 whether DRP1 and BAX closely interact in the axon after injury. One hour after axotomy, we
278 observed a significant increase in red fluorescence. The interaction between DRP1 and BAX
279 occurred at mitochondria as shown by co-localization with mito-GFP (Fig. 6A). However, DLK
280 inhibitor GNE3511 reduced the interaction (Fig. 6A-B). To test whether the interaction between
281 DRP1 and BAX was dependent on the phosphorylation of DRP1 at S616, we mutated the B_1-DRP
282 construct to carry a S616A point mutation, preventing its phosphorylation at this site. A_1-BAX and
283 B_1-DRP1 S616A did not show the increase in red fluorescence, demonstrating that the interaction
284 between BAX and DRP1 is more likely to occur if DRP1 is phosphorylated at S616 (Fig. 6C), which
285 is mediated by DLK (Fig. 3).
286
287 We next tested whether inhibiting BAX would prevent cell death and axon degeneration in
288 i3Neurons using BAI, a highly selective small molecule inhibitor of BAX[51]. BAX inhibition
289 significantly preserved cell bodies of axotomized neurons (Fig. 6D-E). We also found that BAX
290 inhibition significantly reduced axon degeneration measured 24 hours after injury (Fig. 6F),
291 indicating that BAX is a key mediator of axon degeneration and cell death after axotomy.
292
293 Finally, we asked whether local activation of BAX in the axon was sufficient to cause axons to
294 degenerate. Other studies have shown stimulation of Bax with a Bcl-x antagonist causes axon
295 degeneration[19,52] . We grew i3Neurons in microfluidic chambers, which physically isolate axons
296 from cell bodies and dendrites, and added BAX activator (BAX-A), which binds to the N-terminus
297 of BAX to promote its oligomerization[53], to the axon compartment. We measured axon integrity
298 24 hours later. We also tested this in the presence of DLK inhibitor GNE3511 (Fig. 6H). Local
299 activation of BAX caused axons to degenerate, independently of DLK inhibition (Fig. 6H-I). These
300 data show that axotomy-induced degeneration relies on BAX as well as DRP1 and DLK, and reveal
301 that these proteins interact in a signaling cascade. Upon axotomy, DLK directly phosphorylates
302 DRP1 at S616, which facilitates the interaction between DRP1 and BAX in axonal mitochondria
303 and leads to BAX-dependent apoptosis.
304
305
306 **Discussion**
307 In this work, we establish a novel and reproducible model of progressive axon degeneration and
308 neuronal death in human neurons and unravel a cascade of events governing neurodegeneration
309 after axon injury. We show that DLK directly phosphorylates DRP1 to drive mitochondrial fission
310 and BAX-dependent apoptosis that originates in the axon and leads to degeneration of the axon

311 followed by the cell body. We demonstrate the relevance of this pathway *in vivo*, extending from
312 cultured human neurons to retinal ganglion cells of mice with optic nerve crush injuries. We
313 hypothesize this pathway is broadly implicated in neuronal degeneration caused by axon
314 damage, such as spinal cord injury and traumatic brain injury.
315
316 While BAX and DLK have separately been implicated in neuronal apoptosis of retinal ganglion
317 cells after optic nerve crush[26,45,54,55], an interaction between the two has not previously been
318 reported, nor with DRP1. One study reported that DRP1-dependent mitochondrial fission occurs
319 in axons after damage[56]. Here, we show how DLK, DRP1, and BAX cooperate to cause neuronal
320 apoptosis after axon damage, and in particular, how the same apoptotic mechanism can follow
321 axon loss[57] .
322
323 Until now, it was also unclear whether pathways distinct from SARM1 can mediate axon
324 degeneration. Many clinical descriptions of axon degeneration refer to "dying back" as a pattern
325 in which distal axons are lost before cell bodies[58,59]. It has been suggested that dying back axon
326 degeneration overlaps with Wallerian degeneration[60], but this remains unclear. Although axon
327 degeneration is rescued by SARM1 deletion in some models (e.g. chemotherapy-induced
328 peripheral neuropathy[61]; TDP43-linked ALS[62]), it is not in others (SOD1 mouse model of ALS[5]; and
329 optic nerve crush[6]). We have shown that a type of non-Wallerian axon degeneration that is more
330 akin to apoptosis can occur after axon damage, and that it spreads retrogradely, similar to a dying
331 back. It is possible that additional axon degeneration pathways also exist.
332
333 Therapeutically targeting this pathway offers multiple options. There is precedence for testing
334 some of these strategies, such as blocking BAX[54,55], or targeting mitochondrial dynamics[63],
335 including promoting mitochondrial fusion[30] and blocking mitochondrial fission[64–67]. Blocking DLK
336 signaling using small molecules has been considered[68–70], although a Phase I clinical trial in ALS
337 patients was recently halted due to safety concerns[71]. However, specifically targeting the
338 interaction between DLK and DRP1 has never been attempted.
339
340 In addition to protecting axons as we have shown, targeting DRP1 has the potential to protect
341 dendrites[72] . However, it also has possible issues of toxicity as mitochondrial fission is critical for
342 regeneration and motor neuron survival after sciatic nerve injury[73]. A more complete
343 understanding of DRP1 regulation in homeostatic and injury conditions will be helpful. For
344 example, future studies may identify other targetable DRP1 phosphorylation sites in addition to
345 serine 616 as well as additional kinases. To date, kinases of DRP1 that have been identified
346 include CDK5[74,75], TBK1[76], ERK1/2[77,78] CAMKIα[79] and CAMK2[80]; here, we highlight DLK as a novel
347 DRP1 kinase.
348
349 As a cytoplasmic facing kinase, DLK has the potential to regulate many substrates in addition to
350 MKK4 and MKK7[81] which had been described for canonical DLK signaling, and DRP1 which we
351 now identify. Based in its localization, DLK likely has many substrates and regulators, and these
352 will be of great interest to uncover as well as the functions of these interactions. DLK is reported
353 to associate with the plasma membrane, Rab3, Rab6, Rab7, Rab11, Golgi-derived, and LAMP1-
354 positive vesicles[39,82]. Localization of DLK to mitochondria has also just recently been described in

355 cultured mouse embryonic DRG neurons[82], corroborating our observation of DLK-mitochondrial
356 association.
357
358 Our study highlights a novel signaling pathway downstream of DLK. It has generally been thought
359 that DLK-dependent transcriptional events govern neuronal death [26]. Future studies will
360 determine whether dying-back and/or apoptosis are independent of the transcriptional response
361 or whether one or both of these processes requires both the DLK/DRP1/fission cascade and the
362 DLK-mediated transcriptional response. It will be interesting to examine how the local
363 mitochondrial mechanism we have uncovered for DLK is coordinated with transcriptional
364 regulation of cell death factors by DLK, for example BID and PUMA[19].
365
366 DRP1-dependent apoptosis has been described in many cell types[15]. The real novelty here lies in
367 the activation of DRP1 by DLK, and how axonal DLK can trigger this apoptotic pathway in neurons.
368 Our results call to mind new questions, such as how is DLK localized to the site of mitochondrial
369 fission so it can regulate DRP1 phosphorylation? Does it associate with factors like MFF, which is
370 an essential factor in recruiting DRP1 to mitochondria[83]? And what is the mechanism of activation
371 of DLK that would link it to mitochondrial fission? In the future, it will be of great interest to
372 explore under which conditions this pathway is activated, as well as the specificity of this pathway
373 to different neuronal subtypes.
374

375 **Methods**
376
377 **I3Neuron differentiation**
378 I3Neurons were differentiated as previously described. Briefly, i^3 iPSCs were dissociated using
379 Accutase (Life Technologies, cat. no. A1110501). Cells were plated in Matrigel-coated (1:100
380 Corning) plates in Neuronal induction media on day 0 (Knockout Dulbecco's modified Eagle's
381 medium (DMEM)/F12 medium; Life Technologies Corporation, cat. no. 12660012), 1X N2
382 supplement (Life Technologies, cat. no. 17502048), 1× GlutaMAX (Thermofisher Scientific, cat.
383 no. 35050061), 1× MEM nonessential amino acids (NEAA) (Thermofisher Scientific, cat. no.
384 11140050), 10 µM ROCK inhibitor (Y-27632; Selleckchem, cat. no. S1049), and 2 µg/ml
385 doxycycline (Clontech, cat. no. 631311). Neuronal induction media was changed once a day for 2
386 more days. On day 3 of induction, cells were dissociated using Accutase and plated in dishes
387 coated with poly-L-ornithine (PLO; 0.1 mg/ml; Sigma, cat. no. P3655-10MG). Cells were plated in
388 neuronal maturation media (BrainPhys medium (STEMCELL Technologies, cat. no. 05790), 1× B27
389 Plus Supplement (ThermoFisher Scientific, cat. no. A3582801), 10 ng/ml BDNF (PeproTech, cat.
390 no. 450-02), 10 ng/ml NT-3 (PeproTech, cat. no. 450-03), 1 mg/ml mouse laminin (Invitrogen, cat.
391 no. 23017015), and 2 µg/ml doxycycline). Half of the neuronal maturation media was removed
392 and replenished with fresh media every 2-3 days.
393
394 **DRP1 knockdown using dead Cas9**
395 For DRP1 knockdown, we used CRISPRi-i^3 iPSCs containing a CAG promoter-driven dCas9-BFP-
396 KRAB cassette inserted into the CLYBL safe harbor locus (Addgene #127968). iPSCs were
397 transduced with control gRNA or a previously validated gRNA targeting DRP1[84] and differentiated
398 as described above.
399
400 **Laser Axotomies**
401 Laser Axotomies were performed on 10-14 day old neurons using a Zeiss LSM 880 Upright 2-
402 Photon microscope equipped with an ablate laser. Temperature and CO_2 levels were maintained
403 using a Pecon microscope incubator. Ablation laser was set to 800 nm, 100% power and 100
404 iterations. Neurons were cultured in µ-Dish 35 mm dishes (Ibidi, Cat. No. 81156 or 81166
405 depending on the application) in Hybernate E (Gibco, Cat. No. A1247601), 1× B27 Plus
406 Supplement (ThermoFisher Scientific, cat. no. A3582801), 10 ng/ml BDNF (PeproTech, cat. no.
407 450-02), 10 ng/ml NT-3 (PeproTech, cat. no. 450-03), 1 mg/ml mouse laminin (Invitrogen, cat. no.
408 23017015), and 2 µg/ml doxycycline.
409
410 **Mitochondrial fission after axotomy**
411 iPSCs were differentiated as described above. On day 1 of differentiation, cells were transduced
412 with the appropriate lentivirus. Neuronal induction media was changed 24 hours later. On day 3
413 of differentiation, 50,000 cells were plated in a 5 µL drop of neuronal maturation media in the
414 middle of a 35mm dish (ibidi, Cat. No. 81156) for the axons to grow out from the center. Dishes
415 were incubated for 20 minutes at 37°C to allow cells to attach, and 2mL of neuronal maturation
416 media was then added to each well. Cells were fed with half-media changes every two days until
417 the day of the experiment. Laser axotomies were performed as described above. Single axons
418 were randomly selected. Five images were taken before axotomy every 5 seconds and axons

419 were imaged for 5 minutes after axotomy every 5 seconds. The number of mitochondrial particles
420 was quantified using imageJ imaging software and normalized to the number of mitochondria
421 pre-axotomy. When treating neurons with different chemical compounds, neurons were
422 pretreated for one hour prior to performing axotomies. The following compounds were used
423 GNE3511 (500 nM, Sigma, Cat. No. 5331680001), P110 (1 µM, Tocris, Cat. No. 6897), BAPTA-AM
424 (10mM Tocris, Cat. No. 2787), BSTA1 (BAX activator, 10 µM, Sigma, Cat. No. SML2243) and BAI1
425 (BAX inhibitor, 10 µM, Medchemexpress, Cat. No. HY-103269).
426
427 **Axon separation and axotomies**
428 For axon separation experiments after axotomy, 1.5 million cells were plated in 150 µl of
429 maturation media in a strip in the center of a 6 cm dish. Cells were allowed to attach for 15
430 minutes at 37°C, after which 8 ml of media was added to the dish. Neurons were cultured for 1
431 month to allow for the axons to project outwards. Axotomy was performed using a sharp blade.
432 Axons and cell bodies were separated and processed for western blotting.
433
434 **Immunostaining**
435 Cells were fixed in cold 4% PFA for 5-10 minutes, permeabilized using 0.1% TritonX in PBS for 5
436 mins and blocked in 5% normal donkey serum (NDS) in PBS at room temperature for 1 hour. Cells
437 were immunostained with the selected primary antibody in 2.5% NDS overnight at 4°C. Cells were
438 washed three times with PBS and stained with the appropriate secondary antibody at a
439 concentration of 1:500 in 2.5% NDS for 1 hour at room temperature. Cells were washed three
440 times with PBS and DAPI was used as a nuclear counterstain. Antibodies used: βIII tubulin
441 (Thermo Fischer, cat. no. 2G10, 1:500), anti-pDRP1 S637 (CST, cat. no. 4867S, 1:1000), DLK (CST,
442 cat. no. GF-32-1, 1:500), TOMM20 (Santa Cruz, cat. no. SC-17764, 1:500).
443
444 **Calcium imaging**
445 Neurons were plated as described above in the center of a 35mm dish, and their axons were
446 allowed to grow outwards. 10-14 days post induction, neurons were treated with Fluo-4 AM cell
447 permeable calcium dye (ThermoFischer, Cat. No. F14201) following the manufacturers
448 indications. Axotomies were performed on single axons as described above and imaged every 2
449 seconds for 2 minutes after axotomy. Fluorescence intensities were calculated using ImageJ
450 software and normalized to pre-axotomy levels.
451
452 **HEK cell culture and transfection**
453 HEK-293T cells were cultured in DMEM (Gibco, cat. no 11995065) supplemented with 10% FBS
454 (Gibco; cat. no. 10437028). For transfection, cells were dissociated using Trypsin-EDTA (0.25%)
455 (ThermoFischer, Cat. No. 25200056) and plated in DMEM, 10%FBS. The day after plating cells
456 were transfected with 1 µg DNA plasmid, 8 µl lipofectamine 2000 (Invitrogen, Cat. No. 11668030)
457 for 24 hours. For western blotting, cells were harvested in ice cold RIPA buffer (Invitrogen, cat.
458 no. 89901) supplemented with protease inhibitors (Sigma, 11836153001) and PhosStop (Sigma
459 cat. no. 4906845001). For immunostaining, cells were fixed in 4% PFA for 10 minutes.
460
461 **Western blotting**

462 Protein concentrations were calculated using a BCA assay (ThermoFisher, cat. no. 23225). 10-20
463 µg of total protein lysate was loaded into a 4–20% Mini-PROTEAN® TGX™ Precast Protein Gels
464 (Biorad, cat. no. 4561095). Gels were transferred into PVDF membranes and blocked for 1 hour
465 at room temperature in 5% BSA. Membranes were incubated with the appropriate primary
466 antibody in 2.5% BSA solution in a cold room, rocking, overnight. Membranes were washed 3
467 times with PBS 0.1% Tween solution. Secondary antibody was incubated for 1 hour at room
468 temperature at a concentration of 1:8000 in 2.5% BSA solution. Membranes were washed 3 times
469 with PBS 0.1% Tween solution prior to developing. Western blots were developed using Clarity
470 Western ECL Substrate (Biorad, cat. no. 1705061) and imaged using a ChemiDoc MP Imaging
471 system (Biorad). Band intensity was quantified using FIJI imaging analysis software. The following
472 antibodies were used at the concentrations stated: anti-DRP1 (Santa Cruz Biotechnology, cat. no.
473 sc-101270, 1:1000), anti-pDRP1 S616 (CST, cat. no. 3455S, 1:1000), anti-ß Actin (Sigma, cat. no.
474 A1978, 1:5000), anti-p-cJun S63 (CST, cat. no. 9261, 1:1000), anti-pDRP1 S637 (CST, cat. no.
475 4867S, 1:1000).
476
477 **Axon Degeneration index and neuron survival**
478 Induction of iPSCs into neurons was performed as described above. On day 1 of differentiation,
479 neurons were transduced with a cytoplasmic mApple (cyto mApple)-expressing lentivirus, and
480 the media was changed 24 hours later. On day 3 of differentiation, transduced neurons were
481 mixed with mixed with untransduced neurons at a ratio of 1:8000 to achieve sparse labelling of
482 neurons, and re-plated on a 35mm gridded dish (Ibidi Cat. No. 81166). On day 14 of
483 differentiation, the positions of selected axons or neuron somas was recorded and laser
484 axotomies were performed as described above. Dished were stored in a temperature and CO_2
485 controlled incubator until imaged next. Injured axons and somas were re-located at different
486 time points after axotomy using the gridded dish and imaged. Axons were injured <1mm away
487 from the soma. The axon degeneration index was calculated as previously described[33].
488
489 **Airyscan imaging**
490 Neurons were plated in 1mm German Glass Coverslips thickness #1.5 (Electron Microscopy
491 Sciences, Cat. No. 72290-04). 10-day old neurons were fixed with 4% PFA for 10 minutes at
492 room temperature. Cells were permeabilized with 0.1% Triton-X for 5 minutes and blocked in
493 5% normal donkey serum (NDS) at room temperature for an hour. Primary antibody incubation
494 was carried out in 2.5% NDS overnight at 4°C. Cells were washed three times with PBS and
495 stained with the appropriate secondary antibody at a concentration of 1:500 in 2.5% NDS for 1
496 hour at room temperature. Cells were washed three times with PBS and DAPI was used as a
497 nuclear counterstain. Coverslips were mounted using ProLong Glass antifade (Invitrogen, Cat.
498 No. P36980).
499
500 **Seahorse analysis**
501 For Seahorse analysis, 50,000 cells per well were plated after 3 days of induction in a specialized
502 Seahorse analyzer 96-well plate (Agilent, cat. no. 103774-100). Cells were washed in PBS once
503 and incubated in a hypoxic chamber following the manufacturer's procedure. Seahorse analysis
504 was performed using a Seahorse XFe 96 Analyzer (Agilent). The average value for three wells was
505 used for analysis.

506 **Protein purification and *in vitro* kinase assay**
507 DLK and DRP1 were cloned into a pcDNA3-C-terminal GST vector. 12 million HEK293 cells were
508 plated in 10 cm dished coated with Matrigel. The day after, cells were transfected with 10 µg
509 plasmids and 40 µl lipofectamine. 24 hours post transfection, cells were washed twice with PBS
510 and harvested in 880 µl ice cold RIPA buffer (Invitrogen, cat. no. 89901) supplemented with
511 protease inhibitors (Sigma, 11836153001) and PhosStop (Sigma cat. no. 4906845001). Lysates
512 were sonicated and spun at 18000g 10 minutes at 4°C and the pellet was discarded. 500 µl
513 Glutathione-Sepharose beads (Sigma Cat. No. GE17-0756-01) were washed twice in 1ml in lysis
514 buffer. Washed beads to 1 ml lysate and incubate end-over-end shaking in cold room overnight.
515 The next morning. Beads were washed 4 times with lysis buffer + 0.4M NaCl. The protein-
516 containing beads were pelleted by spinning 1min 8000rpm at 4°C, the supernatant was
517 discarded, and the beads were resuspended in fresh 200 mM glutathione 1X PBS solution for
518 elution of the desired protein. The beds were incubated for 20 minutes at room temperature
519 shaking. The eluted protein and the beads were separated by briefly spinning in a SpinX column
520 tubes (Sigma Cat. No. CLS8162-24EA). The purity of purified protein was by running 5 µg of
521 protein on an SDS PAGE gel and performing Comassie stain. The purified protein was stored at -
522 80°C. For *in vitro* kinase assay, purified GST-DLK or GST-DLK-S302A was mixed with purified GST-
523 DRP1 at a 1:1 ratio in 50 µl kinase buffer (50mM TrisHCL pH 7.5, 150mM NaCl, 10mM MgCl,
524 10mM $MnCl_2$, 1.8mM ATP) incubated for 60 mins at 37 °C. The reaction was terminated by adding
525 SDS gel loading buffer and the sample was subjected to western blotting.
526
527 **Phospho-mass spectrometry**
528 DRP1 bands, with ~0.5 µg protein on each band, were cut from SDS-PAGE. In-gel samples were
529 reduced with 10 mM Tris(2-carboxyethyl)phosphine hydrochloride, alkylated with N-
530 Ethylmaleimide, and digested with trypsin at 37°C for 18 hours. Peptides were extracted,
531 desalted and injected into a nano-LC-MS/MS system where an Ultimate 3000 HPLC was coupled
532 to an Orbitrap Lumos mass spectrometer (Thermo Scientific) via an Easy-Spray ion source
533 (Thermo Scientific). Peptides were separated on an ES902 Easy-Spray column (75-µm inner
534 diameter, 25 cm length, 3 µm C18 beads; Thermo Scientific) with mobile phase B (0.1% formic
535 acid in LC-MS grade acetonitrile) increased from 3% to 24% in 60 min. The flow rate was
536 maintained at 300 nl/min. MS and MS/MS data were acquired on Thermo Scientific Orbitrap
537 Lumos mass spectrometer. MS1 scans were acquired in orbitrap at of a resolution 120k with a
538 mass range of m/z 400-1500. MS2 scans were acquired in ion trap with ETciD method at normal
539 scan rate. The isolation width was 1.6 m/z. Ions were excluded after 1 acquisition and the
540 exclusion duration is 9 sec. MS1 scans were performed every 3 sec. As many MS2 scans were
541 acquired within each MS1 scan cycle.
542 Proteome Discoverer software version 2.4 was used for protein identification and quantitation.
543 Database search was performed against Sprot Human database using Mascot search engine.
544 Mass tolerances for MS1 and MS2 scans were set to 5 ppm and 0.4 Da, respectively. Up to 2
545 missed cleavage was allowed for trypsin digestion. NEM on cysteines was set as fixed
546 modification. Oxidation (M) and Phosphorylation (STY) were searched as variable modifications.
547 Spectra of phosphopeptides matched by database search were manually checked. The search
548 results were filtered by a false discovery rate of 1% at the protein level. Proteins detected with
549 1-2 peptides were further filtered out. Protein abundance values were calculated by summing

550 the abundance of unique and razor peptides matched to that protein. Each sample group
551 contains 4 replicates. The ratios were calculated using protein abundance without normalization.
552
553 **Electron microscopy**
554 Neurons were plated in 1mm German Glass Coverslips thickness #1.5 (Electron Microscopy
555 Sciences, Cat. No. 72290-04). 10 Day old neurons were fixed with in 4% PFA, 1% Glutaraldehyde
556 for 40 minutes. Fixed cells were placed in phosphate buffer containing 0.1% sodium borohydride
557 to inactivate residual aldehyde groups. Cells were then washed with phosphate buffer several
558 times until the solution was clear of bubbles. To improve reagent penetration, the cells were then
559 treated with phosphate buffer containing 0.05% Triton X-100. To prevent nonspecific binding of
560 the immunoreagents, cells were incubated in Aurion blocking solution for Goat gold conjugates
561 (Electron Microscopy Sciences, Hatfield, PA., containing phosphate buffer, pH 7.4, normal goat
562 serum (NGS), bovine serum albumin (BSA), and cold water fish skin gelatin (CWFG)). After
563 blocking, cells were incubated in the primary antibody, Rabbit anti-DLK (1:100), (Sigma-Aldrich,
564 St. Louis, MO) diluted with incubation buffer (phosphate buffer containing 0.2% Aurion
565 acetylated bovine serum albumin (BSA-c), Electron Microscopy Sciences, Hatfield, PA., 5% CWFG
566 and 5% NGS, pH 7.4) for two hours at room temperature. After washes with incubation buffer,
567 cells were incubated in the secondary antibody Aurion ultra-small gold-conjugated
568 $F(ab')_2$ fragments of Goat anti-Rabbit IgG, (Electron Microscopy Sciences, Hatfield, PA.) diluted
569 1:100 with incubation buffer overnight at 4^oC. To remove unbound secondary antibody, cells
570 were washed thoroughly with incubation buffer and then with PBS. After washes, cells were
571 prepared for silver enhancement.
572
573 **Silver Enhancement and Cell processing for Electron Microscopy**
574 Cells were washed with MilliQ water and then transferred to Aurion R-Gent SE-EM silver
575 enhancement solution, Electron Microscopy Sciences, Hatfield, PA. and incubated at room
576 temperature for 35 minutes. The enhancement was stopped by washing cells several times in
577 MilliQ water. The following processing steps were carried out using the variable wattage Pelco
578 BioWave Pro microwave oven (Ted Pella, Inc., Redding, CA.): cells were rinsed in MilliQ water,
579 post-fixed in 1% osmium tetroxide made in MilliQ water, ethanol dehydration series up to 100%
580 ethanol, followed by a Embed-812 resin (Electron Microscopy Sciences, Hatfield, PA.) infiltration
581 series up to 100% resin. The epoxy resin was polymerized for 20 hours in an oven set at 60°C.
582 Ultra-thin sections (90nm) were prepared on a Leica EM UC7 ultramicrotome. Ultra-thin sections
583 were picked up and placed on 200-mesh cooper grids (Electron Microscopy Sciences, Hatfield,
584 PA) and post-stained with uranyl acetate and lead citrate. Imaging was performed on a JEOL-1400
585 Transmission Electron Microscope operating at 80kV and images were acquired on an AMT
586 BioSprint 29 camera.
587
588 **Generation of DLK KO iPSCs**
589 WT iPSCs were transfected with Cas9-GFP, and two gRNA containing plasmids targeting exons 3
590 and 5. gRNA expressing plasmids were purchased from Sigma Aldrich (U6-gRNA:hPGK-puro-2A-
591 tBFP, gRNA1: CCCAGGCTCCCTGCTACTGCAT, gRNA 2: TCCTTTGGCGTGGTGCTATGGG). 1 day after
592 transfection, expression of Cas9 and gRNAs was validated by the expression of GFP and BFP
593 respectively and iPSCs were treated for 3 days with 10 µM Puromycin (Invitrogen Cat. No.

A11113803) and allowed to recover for 3 days. Cells were then dissociated with accutase for 10 minutes and dissociated my pipetting forcefully 10 times. A 1:2 serial dilution was then performed in two 6 well plates. iPSCs were fed every 3 days until individual colonies were visible (usually 10-14 days). Individually colonies were picked using a P1000 pipette and transferred into individual wells in a 24-well plate. Individual clones were allowed to expand, passaged and their DNA was extracted for DLK KO validation using PCR (Forward primer: TCAGGTGAATGCTGAGCCAGCT, reverse primer: TGGAGACTGTTGCTTCCCACAC). A shorter band from ~1200bp to ~200bp was expected if the KO was successful. Potential clones were sequenced. Further validation was performed by differentiating potential clones into neurons and knock out of DLK was validated by western blotting.

Animals

All animal care and experimental procedures were performed in accordance with animal study proposals approved by the National Institute of Child Health and Human Disease Animal Care and Use Committee (animal protocol number 20-003, Le Pichon lab) and by the Baylor College of Medicine ACUC (animal protocol #AN-7208; Watkins lab). C57Bl/6J (Jax#000664) mice of both sexes, aged between 6-10 weeks old, were used in this study.

Mouse tissue preparation

The proximal segment of the injured nerve was harvested, and 4 nerves were pooled to obtain enough protein. Nerves were mechanically lysed in 40 µl ice cold RIPA buffer (Invitrogen, cat. no. 89901) supplemented with protease inhibitors (Sigma, 11836153001) and PhosStop (Sigma cat. no. 4906845001) for 2 minutes using a micro pestle. Nerves were then sonicated for 15 minutes at 4°C. Protein lysates were centrifuged at 18 000g, 4°C for 10 minutes and the pellet was discarded. The samples were subjected to the western blotting procedure described above. Abundance of phopho-DRP1/ total DRP1 was obtained running two western blots. Phosphorylated and unphosphorylated protein was divided by the total protein and then divided to each other to obtain the relative levels of phosphorylated protein.

Adeno-associated virus (AAV)

Adeno-associated viral vectors carrying human synapsin-1 (*hSyn1*) promoter driving expression of saCas9-U6-control, saCas9-U6-DRP1-gRNA, or eGFP were generated by Epoch Life Sciences Inc. The plasmids were then packaged into AAV2 capsids at the Optogenetics and Viral Vector Core at Duncan Neurological Research Institute, Houston.

Intravitreal injections

Mice to be injected were anesthetized with 3% isoflurane. The eyes were sterilized by 3 repeated applications of 5% ophthalmic betadine (Henry Schein #6900250), Opti-clear ophthalmic eye wash (Akorn #NDC 17478-620-04) and a dry wipe. A topical anesthetic 0.5% proparacaine HCl ophthalmic solution (Henry Schein #1365345) was applied. The eyeball was punctured using a 5-µl Hamilton syringe loaded with a custom 33-gauge needle (Hamilton #7803-5) and some of the intraocular pressure was relieved. The same puncture site was used to reinsert the Hamilton needle and 2 µl of AAV in titers ranging from 10^{12} -10^{13} vg/ml was delivered per eye.

638 **Intra-orbital optic nerve crush (ONC)**
639 Two weeks after intravitreal injections, animals underwent optic nerve crush surgeries. Mice
640 undergoing surgery were dosed with 1mg/kg buprenorphine sustained release formulation 1
641 hour before surgery. Right before surgery, mice were anesthetized with 3% isoflurane. The non-
642 surgical eye received artificial tears ointment (Covetrus #11695-6832-1. The surgical eye was
643 sterilized as described in the intravitreal injections section above. Topical anesthetic 0.5%
644 proparacaine HCl ophthalmic solution (Henry Schein #1365345) was applied on the surgical eye
645 (left). A pair of Vannas scissors (World precision instruments #501777) were used to make
646 incisions in the conjunctival layers. The optic nerve section in the intra-orbital space was exposed
647 by using two pairs of suture-tying forceps (Fine science tools #1106307) to gently clear the soft
648 tissue behind the eye until the optic nerve was visible. The optic nerve was manually crushed for
649 5s by using a pair of Dumont forceps (Fine science tools #1125325). The eyeball was gently placed
650 back into the orbit. Animals were post-surgically monitored in their home cages until sternal
651 recumbency was observed.
652
653 **Immunolabeling of retinae**
654 At the experimental endpoint (3 days after optic nerve crush) mice were euthanized by an
655 overdose of isoflurane and followed by decapitation. The eyes were enucleated and drop-fixed
656 in 4% paraformaldehyde for 1 hour. The retinae were dissected out in 1X phosphate-buffered
657 saline (PBS) and then blocked with blocking buffer (5% goat serum, 0.5% Triton X-100 and 0.025%
658 sodium azide in 1X PBS) for 30min. The retinae were then immersed in primary antibody solution
659 prepared by dilution in blocking buffer solution and incubated for 5 days in 4◦C. They were then
660 washed three times in 1X PBS with 0.5% TritonX-100 for 30 min each, and then moved to
661 appropriate secondary antibody solution prepared in blocking buffer and incubated overnight in
662 4◦C. After secondary antibody incubation, they were washed again three times in 1X PBS with
663 0.5% TritonX-100 for 30 min each. Retinae were then mounted in Drop-n-Stain EverBrite™
664 Mounting Medium (Biotium #23008) onto slides and imaged using Zeiss Axio Imager Z1
665 fluorescence microscope.
666
667 **DLK inhibitor treatment**
668 GNE-3511 solution was synthesized as previously described[68]. Briefly, GNE-3511 was dissolved in
669 a solution of 0.5% w/v USP Grade Methyl Cellulose and 0.2% v/v Tween 80 in water up to 48
670 hours before dosing. Mice were dosed by oral gavage every 12 hours at 75 mg/kg with 10 ml/kg
671 body weight of a 7.5 mg/ml solution of GNE-3511 or vehicle alone.
672
673
674
675 **Funding**
676 This work was supported by NIH intramural funding NICHD ZIA-HD008966 (CLP), by a Milton-
677 Safenowitz postdoctoral fellowship from the ALS Association (JG-D), by NIH grant R01NS112691
678 (TAW) and grant #021-107 from Mission Connect, a project of the TIRR Foundation (TAW), and
679 NIH intramural funding NINDS 1ZIANS003155-03 (MEW).
680
681

682 **Acknowledgements**
683 We would like to thank Drs. Vincent Schram and Chip Dye and the NICHD Microscopy core, Dr.
684 Yan Li and the NINDS proteomics core, the NHLBI FACS core facility staff, and Dr. Gareth
685 Thomas (Temple University) for reagents. We would also like to thank members of Dr. Michael
686 Ward's lab for advice, and Dr. Nicholas Ryba, Dr. Richard Youle, Dr. David Simon, Dr. Alexander
687 Chesler, and Dr. Joseph Lewcock for helpful discussion and comments on the manuscript.
688
689
690 **Author contributions**
691 Conceptualization: JGD and CLP.
692 Methodology and Investigation: all authors.
693 Formal Analysis: MN and JGD.
694 Visualization: JGD and CLP.
695 Writing: JGD and CLP.
696 Supervision: CLP, TW, MEW.
697 Funding acquisition: CLP, TW, MEW.

698 **References**
699

700 1. Whitmore, A.V., Lindsten, T., Raff, M.C., and Thompson, C.B. (2003). The proapoptotic
701 proteins Bax and Bak are not involved in Wallerian degeneration. Cell Death Differ *10*, 260–261.
702 10.1038/sj.cdd.4401147.

703 2. Deckwerth, T.L., Elliott, J.L., Knudson, C.M., Johnson, E.M., Snider, W.D., and Korsmeyer, S.J.
704 (1996). BAX Is Required for Neuronal Death after Trophic Factor Deprivation and during
705 Development. Neuron *17*, 401–411. 10.1016/s0896-6273(00)80173-7.

706 3. Osterloh, J.M., Yang, J., Rooney, T.M., Fox, A.N., Adalbert, R., Powell, E.H., Sheehan, A.E.,
707 Avery, M.A., Hackett, R., Logan, M.A., et al. (2012). dSarm/Sarm1 Is Required for Activation of
708 an Injury-Induced Axon Death Pathway. Science *337*, 481–484. 10.1126/science.1223899.

709 4. Gerdts, J., Brace, E.J., Sasaki, Y., DiAntonio, A., and Milbrandt, J. (2015). SARM1 activation
710 triggers axon degeneration locally via NAD^+ destruction. Science *348*, 453–457.
711 10.1126/science.1258366.

712 5. Peters, O.M., Lewis, E.A., Osterloh, J.M., Weiss, A., Salameh, J.S., Metterville, J., Brown, R.H.,
713 and Freeman, M.R. (2018). Loss of Sarm1 does not suppress motor neuron degeneration in the
714 SOD1G93A mouse model of amyotrophic lateral sclerosis. Hum Mol Genet.
715 10.1093/hmg/ddy260.

716 6. Fernandes, K.A., Mitchell, K.L., Patel, A., Marola, O.J., Shrager, P., Zack, D.J., Libby, R.T., and
717 Welsbie, D.S. (2018). Role of SARM1 and DR6 in retinal ganglion cell axonal and somal
718 degeneration following axonal injury. Exp Eye Res *171*, 54–61. 10.1016/j.exer.2018.03.007.

719 7. Mandal, A., and Drerup, C.M. (2019). Axonal Transport and Mitochondrial Function in
720 Neurons. Front Cell Neurosci *13*, 373. 10.3389/fncel.2019.00373.

721 8. Smith, G.M., and Gallo, G. (2018). The role of mitochondria in axon development and
722 regeneration. Dev Neurobiol *78*, 221–237. 10.1002/dneu.22546.

723 9. Han, S.M., Baig, H.S., and Hammarlund, M. (2016). Mitochondria Localize to Injured Axons to
724 Support Regeneration. Neuron *92*, 1308–1323. 10.1016/j.neuron.2016.11.025.

725 10. Lin, M.-Y., Cheng, X.-T., Tammineni, P., Xie, Y., Zhou, B., Cai, Q., and Sheng, Z.-H. (2017).
726 Releasing Syntaphilin Removes Stressed Mitochondria from Axons Independent of Mitophagy
727 under Pathophysiological Conditions. Neuron *94*, 595-610.e6. 10.1016/j.neuron.2017.04.004.

728 11. Karbowski, M., and Youle, R.J. (2003). Dynamics of mitochondrial morphology in healthy
729 cells and during apoptosis. Cell Death Differ *10*, 870–880. 10.1038/sj.cdd.4401260.

730 12. Palau, F., Estela, A., Pla-Martín, D., and Sánchez-Piris, M. (2009). Inherited Neuromuscular
731 Diseases, Translation from Pathomechanisms to Therapies. Adv Exp Med Biol *652*, 129–137.
732 10.1007/978-90-481-2813-6_9.

733 13. Tilokani, L., Nagashima, S., Paupe, V., and Prudent, J. (2018). Mitochondrial dynamics:
734 overview of molecular mechanisms. Essays Biochem *62*, 341–360. 10.1042/ebc20170104.

735 14. Youle, R.J., and Bliek, A.M. van der (2012). Mitochondrial Fission, Fusion, and Stress. Science
736 *337*, 1062–1065. 10.1126/science.1219855.

737 15. Lee, Y., Jeong, S.-Y., Karbowski, M., Smith, C.L., and Youle, R.J. (2004). Roles of the
738 Mammalian Mitochondrial Fission and Fusion Mediators Fis1, Drp1, and Opa1 in Apoptosis. Mol
739 Biol Cell *15*, 5001–5011. 10.1091/mbc.e04-04-0294.

740 16. Frank, S., Gaume, B., Bergmann-Leitner, E.S., Leitner, W.W., Robert, E.G., Catez, F., Smith,
741 C.L., and Youle, R.J. (2001). The Role of Dynamin-Related Protein 1, a Mediator of Mitochondrial
742 Fission, in Apoptosis. Dev Cell *1*, 515–525. 10.1016/s1534-5807(01)00055-7.

743 17. Milani, M., Beckett, A.J., Al-Zebeeby, A., Luo, X., Prior, I.A., Cohen, G.M., and Varadarajan, S.
744 (2019). DRP-1 functions independently of mitochondrial structural perturbations to facilitate
745 BH3 mimetic-mediated apoptosis. Cell Death Discov *5*, 117. 10.1038/s41420-019-0199-x.

746 18. Jenner, A., Peña-Blanco, A., Salvador-Gallego, R., Ugarte-Uribe, B., Zollo, C., Ganief, T.,
747 Bierlmeier, J., Mund, M., Lee, J.E., Ries, J., et al. (2022). DRP1 interacts directly with BAX to
748 induce its activation and apoptosis. Embo J *41*, e108587. 10.15252/embj.2021108587.

749 19. Simon, D.J., Pitts, J., Hertz, N.T., Yang, J., Yamagishi, Y., Olsen, O., Tešić Mark, M., Molina, H.,
750 and Tessier-Lavigne, M. (2016). Axon Degeneration Gated by Retrograde Activation of Somatic
751 Pro-apoptotic Signaling. Cell *164*, 1031–1045. 10.1016/j.cell.2016.01.032.

752 20. Simon, D.J., Weimer, R.M., McLaughlin, T., Kallop, D., Stanger, K., Yang, J., O'Leary, D.D.M.,
753 Hannoush, R.N., and Tessier-Lavigne, M. (2012). A Caspase Cascade Regulating Developmental
754 Axon Degeneration. J Neurosci *32*, 17540–17553. 10.1523/jneurosci.3012-12.2012.

755 21. Tian, R., Gachechiladze, M.A., Ludwig, C.H., Laurie, M.T., Hong, J.Y., Nathaniel, D., Prabhu,
756 A.V., Fernandopulle, M.S., Patel, R., Abshari, M., et al. (2019). CRISPR Interference-Based
757 Platform for Multimodal Genetic Screens in Human iPSC-Derived Neurons. Neuron *104*, 239-
758 255.e12. 10.1016/j.neuron.2019.07.014.

759 22. Liao, Y.-C., Fernandopulle, M.S., Wang, G., Choi, H., Hao, L., Drerup, C.M., Patel, R., Qamar,
760 S., Nixon-Abell, J., Shen, Y., et al. (2019). RNA Granules Hitchhike on Lysosomes for Long-
761 Distance Transport, Using Annexin A11 as a Molecular Tether. Cell *179*, 147-164.e20.
762 10.1016/j.cell.2019.08.050.

763 23. Goldsmith, J., Ordureau, A., Harper, J.W., and Holzbaur, E.L.F. (2022). Brain-derived
764 autophagosome profiling reveals the engulfment of nucleoid-enriched mitochondrial fragments
765 by basal autophagy in neurons. Neuron *110*, 967-976.e8. 10.1016/j.neuron.2021.12.029.

766 24. Fernandopulle, M.S., Prestil, R., Grunseich, C., Wang, C., Gan, L., and Ward, M.E. (2018).
767 Transcription Factor–Mediated Differentiation of Human iPSCs into Neurons. Curr Protoc Cell
768 Biology *79*, e51. 10.1002/cpcb.51.

769 25. Miller, B.R., Press, C., Daniels, R.W., Sasaki, Y., Milbrandt, J., and DiAntonio, A. (2009). A dual
770 leucine kinase–dependent axon self-destruction program promotes Wallerian degeneration.
771 Nat Neurosci *12*, 387–389. 10.1038/nn.2290.

772 26. Watkins, T.A., Wang, B., Huntwork-Rodriguez, S., Yang, J., Jiang, Z., Eastham-Anderson, J.,
773 Modrusan, Z., Kaminker, J.S., Tessier-Lavigne, M., and Lewcock, J.W. (2013). DLK initiates a
774 transcriptional program that couples apoptotic and regenerative responses to axonal injury.
775 Proc National Acad Sci *110*, 4039–4044. 10.1073/pnas.1211074110.

776 27. Huntwork-Rodriguez, S., Wang, B., Watkins, T., Ghosh, A.S., Pozniak, C.D., Bustos, D.,
777 Newton, K., Kirkpatrick, D.S., and Lewcock, J.W. (2013). JNK-mediated phosphorylation of DLK
778 suppresses its ubiquitination to promote neuronal apoptosis. J Cell Biology *202*, 747–763.
779 10.1083/jcb.201303066.

780 28. Pichon, C.E.L., Meilandt, W.J., Dominguez, S., Solanoy, H., Lin, H., Ngu, H., Gogineni, A.,
781 Ghosh, A.S., Jiang, Z., Lee, S.-H., et al. (2017). Loss of dual leucine zipper kinase signaling is
782 protective in animal models of neurodegenerative disease. Sci Transl Med *9*, eaag0394.
783 10.1126/scitranslmed.aag0394.

784 29. Adib, E.A., Smithson, L.J., and Collins, C.A. (2018). An axonal stress response pathway:
785 degenerative and regenerative signaling by DLK. Curr Opin Neurobiol *53*, 110–119.
786 10.1016/j.conb.2018.07.002.

787 30. Franco, A., Dang, X., Zhang, L., Molinoff, P.B., and Dorn, G.W. (2022). Mitochondrial
788 dysfunction and pharmacodynamics of mitofusin activation in murine Charcot-Marie-Tooth
789 disease type 2A. J Pharmacol Exp Ther *383*, JPET-AR-2022-001332. 10.1124/jpet.122.001332.

790 31. Taylor, A.M., Blurton-Jones, M., Rhee, S.W., Cribbs, D.H., Cotman, C.W., and Jeon, N.L.
791 (2005). A microfluidic culture platform for CNS axonal injury, regeneration and transport. Nat
792 Methods *2*, 599–605. 10.1038/nmeth777.

793 32. Tong, Z., Segura-Feliu, M., Seira, O., Homs-Corbera, A., Río, J.A.D., and Samitier, J. (2015). A
794 microfluidic neuronal platform for neuron axotomy and controlled regenerative studies. Rsc
795 Adv *5*, 73457–73466. 10.1039/c5ra11522a.

796 33. Gómez-Deza, J., Slavutsky, A.L., Nebiyou, M., and Pichon, C.E.L. (2022). Local production of
797 reactive oxygen species drives vincristine-induced axon degeneration. Biorxiv,
798 2022.07.30.501173. 10.1101/2022.07.30.501173.

799 34. Court, F.A., and Coleman, M.P. (2012). Mitochondria as a central sensor for axonal
800 degenerative stimuli. Trends Neurosci *35*, 364–372. 10.1016/j.tins.2012.04.001.

801 35. Wang, B., Huang, M., Shang, D., Yan, X., Zhao, B., and Zhang, X. (2021). Mitochondrial
802 Behavior in Axon Degeneration and Regeneration. Front Aging Neurosci *13*, 650038.
803 10.3389/fnagi.2021.650038.

804 36. George, E., Glass, J., and Griffin, J. (1995). Axotomy-induced axonal degeneration is
805 mediated by calcium influx through ion-specific channels. J Neurosci *15*, 6445–6452.
806 10.1523/jneurosci.15-10-06445.1995.

807 37. Villegas, R., Martinez, N.W., Lillo, J., Pihan, P., Hernandez, D., Twiss, J.L., and Court, F.A.
808 (2014). Calcium Release from Intra-Axonal Endoplasmic Reticulum Leads to Axon Degeneration
809 through Mitochondrial Dysfunction. J Neurosci *34*, 7179–7189. 10.1523/jneurosci.4784-
810 13.2014.

811 38. Farley, M.M., and Watkins, T.A. (2018). Intrinsic Neuronal Stress Response Pathways in
812 Injury and Disease. Annu Rev Pathology Mech Dis *13*, 93–116. 10.1146/annurev-pathol-012414-
813 040354.

814 39. Holland, S.M., Collura, K.M., Ketschek, A., Noma, K., Ferguson, T.A., Jin, Y., Gallo, G., and
815 Thomas, G.M. (2016). Palmitoylation controls DLK localization, interactions and activity to
816 ensure effective axonal injury signaling. Proc National Acad Sci *113*, 763–768.
817 10.1073/pnas.1514123113.

818 40. Nihalani, D., Merritt, S., and Holzman, L.B. (2000). Identification of Structural and Functional
819 Domains in Mixed Lineage Kinase Dual Leucine Zipper-bearing Kinase Required for Complex
820 Formation and Stress-activated Protein Kinase Activation*. J Biol Chem *275*, 7273–7279.
821 10.1074/jbc.275.10.7273.

822 41. Longo, D.L., and Archer, S.L. (2013). Mitochondrial Dynamics — Mitochondrial Fission and
823 Fusion in Human Diseases. New Engl J Medicine *369*, 2236–2251. 10.1056/nejmra1215233.

824 42. Ghosh, A.S., Wang, B., Pozniak, C.D., Chen, M., Watts, R.J., and Lewcock, J.W. (2011). DLK
825 induces developmental neuronal degeneration via selective regulation of proapoptotic JNK
826 activity. J Cell Biology *194*, 751–764. 10.1083/jcb.201103153.

827 43. Yu, R., Liu, T., Ning, C., Tan, F., Jin, S.-B., Lendahl, U., Zhao, J., and Nistér, M. (2019). The
828 phosphorylation status of Ser-637 in dynamin-related protein 1 (Drp1) does not determine Drp1
829 recruitment to mitochondria. J Biol Chem *294*, 17262–17277. 10.1074/jbc.ra119.008202.

830 44. Chang, C.-R., and Blackstone, C. (2007). Cyclic AMP-dependent Protein Kinase
831 Phosphorylation of Drp1 Regulates Its GTPase Activity and Mitochondrial Morphology*. J Biol
832 Chem *282*, 21583–21587. 10.1074/jbc.c700083200.

833 45. Welsbie, D.S., Mitchell, K.L., Jaskula-Ranga, V., Sluch, V.M., Yang, Z., Kim, J., Buehler, E.,
834 Patel, A., Martin, S.E., Zhang, P.-W., et al. (2017). Enhanced Functional Genomic Screening
835 Identifies Novel Mediators of Dual Leucine Zipper Kinase-Dependent Injury Signaling in
836 Neurons. Neuron *94*, 1142-1154.e6. 10.1016/j.neuron.2017.06.008.

837 46. Larhammar, M., Huntwork-Rodriguez, S., Jiang, Z., Solanoy, H., Ghosh, A.S., Wang, B.,
838 Kaminker, J.S., Huang, K., Eastham-Anderson, J., Siu, M., et al. (2017). Dual leucine zipper
839 kinase-dependent PERK activation contributes to neuronal degeneration following insult. Elife
840 *6*, e20725. 10.7554/elife.20725.

841 47. Hunker, A.C., Soden, M.E., Krayushkina, D., Heymann, G., Awatramani, R., and Zweifel, L.S.
842 (2020). Conditional Single Vector CRISPR/SaCas9 Viruses for Efficient Mutagenesis in the Adult
843 Mouse Nervous System. Cell Reports *30*, 4303-4316.e6. 10.1016/j.celrep.2020.02.092.

844 48. Robitaille, K., Daviau, A., Lachance, G., Couture, J.-P., and Blouin, R. (2008). Calphostin C-
845 induced apoptosis is mediated by a tissue transglutaminase-dependent mechanism involving
846 the DLK/JNK signaling pathway. Cell Death Differ *15*, 1522–1531. 10.1038/cdd.2008.77.

847 49. Karbowski, M., Lee, Y.-J., Gaume, B., Jeong, S.-Y., Frank, S., Nechushtan, A., Santel, A., Fuller,
848 M., Smith, C.L., and Youle, R.J. (2002). Spatial and temporal association of Bax with
849 mitochondrial fission sites, Drp1, and Mfn2 during apoptosis. J Cell Biology *159*, 931–938.
850 10.1083/jcb.200209124.

851 50. Alford, S.C., Abdelfattah, A.S., Ding, Y., and Campbell, R.E. (2012). A Fluorogenic Red
852 Fluorescent Protein Heterodimer. Chem Biol *19*, 353–360. 10.1016/j.chembiol.2012.01.006.

853 51. Garner, T.P., Amgalan, D., Reyna, D.E., Li, S., Kitsis, R.N., and Gavathiotis, E. (2019). Small
854 Molecule Allosteric Inhibitors of BAX. Nat Chem Biol *15*, 322–330. 10.1038/s41589-018-0223-0.

855 52. Cosker, K.E., Pazyra-Murphy, M.F., Fenstermacher, S.J., and Segal, R.A. (2013). Target-
856 Derived Neurotrophins Coordinate Transcription and Transport of Bclw to Prevent Axonal
857 Degeneration. J Neurosci *33*, 5195–5207. 10.1523/jneurosci.3862-12.2013.

858 53. Reyna, D.E., Garner, T.P., Lopez, A., Kopp, F., Choudhary, G.S., Sridharan, A., Narayanagari,
859 S.-R., Mitchell, K., Dong, B., Bartholdy, B.A., et al. (2017). Direct Activation of BAX by BTSA1
860 Overcomes Apoptosis Resistance in Acute Myeloid Leukemia. Cancer Cell *32*, 490-505.e10.
861 10.1016/j.ccell.2017.09.001.

862 54. Donahue, R.J., Maes, M.E., Grosser, J.A., and Nickells, R.W. (2020). BAX-Depleted Retinal
863 Ganglion Cells Survive and Become Quiescent Following Optic Nerve Damage. Mol Neurobiol
864 *57*, 1070–1084. 10.1007/s12035-019-01783-7.

865 55. Goldenberg-Cohen, N., Dratviman-Storobinsky, O., El, S.D.B., Cheporko, Y., and Hochhauser,
866 E. (2011). Protective Effect of Bax Ablation Against Cell Loss in the Retinal Ganglion Layer
867 Induced by Optic Nerve Crush in Transgenic Mice. J Neuro-ophthalmol *31*, 331–338.
868 10.1097/wno.0b013e318227e4fb.

869 56. Kedra, J., Lin, S., Pacheco, A., Gallo, G., and Smith, G.M. (2021). Axotomy Induces Drp1-
870 Dependent Fragmentation of Axonal Mitochondria. Front Mol Neurosci *14*, 668670.
871 10.3389/fnmol.2021.668670.

872 57. Barrientos, S.A., Martinez, N.W., Yoo, S., Jara, J.S., Zamorano, S., Hetz, C., Twiss, J.L., Alvarez,
873 J., and Court, F.A. (2011). Axonal Degeneration Is Mediated by the Mitochondrial Permeability
874 Transition Pore. J Neurosci *31*, 966–978. 10.1523/jneurosci.4065-10.2011.

875 58. Cavanagh, J.B. (1964). The significance of the “dying back” process in experimental and
876 human neurological disease. Int Rev Exp Pathol *3*, 219–267.

877 59. Yaron, A., and Schuldiner, O. (2016). Common and Divergent Mechanisms in Developmental
878 Neuronal Remodeling and Dying Back Neurodegeneration. Curr Biol *26*, R628–R639.
879 10.1016/j.cub.2016.05.025.

880 60. Coleman, M. (2005). Axon degeneration mechanisms: commonality amid diversity. Nat Rev
881 Neurosci *6*, 889–898. 10.1038/nrn1788.

882 61. Geisler, S., Doan, R.A., Cheng, G.C., Cetinkaya-Fisgin, A., Huang, S.X., Höke, A., Milbrandt, J.,
883 and DiAntonio, A. (2019). Vincristine and bortezomib use distinct upstream mechanisms to
884 activate a common SARM1-dependent axon degeneration program. Jci Insight *4*, e129920.
885 10.1172/jci.insight.129920.

886 62. White, M.A., Lin, Z., Kim, E., Henstridge, C.M., Altamira, E.P., Hunt, C.K., Burchill, E.,
887 Callaghan, I., Loreto, A., Brown-Wright, H., et al. (2019). Sarm1 deletion suppresses TDP-43-
888 linked motor neuron degeneration and cortical spine loss. Acta Neuropathologica Commun *7*,
889 166. 10.1186/s40478-019-0800-9.

890 63. Yang, J., Wu, Z., Renier, N., Simon, D.J., Uryu, K., Park, D.S., Greer, P.A., Tournier, C., Davis,
891 R.J., and Tessier-Lavigne, M. (2015). Pathological Axonal Death through a MAPK Cascade that
892 Triggers a Local Energy Deficit. Cell *160*, 161–176. 10.1016/j.cell.2014.11.053.

893 64. Guo, X., Disatnik, M.-H., Monbureau, M., Shamloo, M., Mochly-Rosen, D., and Qi, X. (2013).
894 Inhibition of mitochondrial fragmentation diminishes Huntington’s disease–associated
895 neurodegeneration. J Clin Invest *123*, 5371–5388. 10.1172/jci70911.

896 65. Joshi, A.U., Saw, N.L., Vogel, H., Cunnigham, A.D., Shamloo, M., and Mochly-Rosen, D.
897 (2018). Inhibition of Drp1/Fis1 interaction slows progression of amyotrophic lateral sclerosis.
898 Embo Mol Med *10*. 10.15252/emmm.201708166.

899 66. Chen, Z., Chai, E., Mou, Y., Roda, R.H., Blackstone, C., and Li, X.-J. (2022). Inhibiting
900 mitochondrial fission rescues degeneration in hereditary spastic paraplegia neurons. Brain.
901 10.1093/brain/awab488.

902 67. Flippo, K.H., Lin, Z., Dickey, A.S., Zhou, X., Dhanesha, N.A., Walters, G.C., Liu, Y., Merrill, R.A.,
903 Meller, R., Simon, R.P., et al. (2020). Deletion of a Neuronal Drp1 Activator Protects against
904 Cerebral Ischemia. J Neurosci *40*, 3119–3129. 10.1523/jneurosci.1926-19.2020.

905 68. Patel, S., Cohen, F., Dean, B.J., Torre, K.D.L., Deshmukh, G., Estrada, A.A., Ghosh, A.S.,
906 Gibbons, P., Gustafson, A., Huestis, M.P., et al. (2015). Discovery of Dual Leucine Zipper Kinase
907 (DLK, MAP3K12) Inhibitors with Activity in Neurodegeneration Models. J Med Chem *58*, 401–
908 418. 10.1021/jm5013984.

909 69. Pichon, C.E.L., Meilandt, W.J., Dominguez, S., Solanoy, H., Lin, H., Ngu, H., Gogineni, A.,
910 Ghosh, A.S., Jiang, Z., Lee, S.-H., et al. (2017). Loss of dual leucine zipper kinase signaling is
911 protective in animal models of neurodegenerative disease. Sci Transl Med *9*, eaag0394.
912 10.1126/scitranslmed.aag0394.

913 70. Siu, M., Ghosh, A.S., and Lewcock, J.W. (2018). Dual Leucine Zipper Kinase Inhibitors for the
914 Treatment of Neurodegeneration. J Med Chem *61*, 8078–8087.
915 10.1021/acs.jmedchem.8b00370.

916 71. Katz, J.S., Rothstein, J.D., Cudkowicz, M.E., Genge, A., Oskarsson, B., Hains, A.B., Chen, C.,
917 Galanter, J., Burgess, B.L., Cho, W., et al. (2022). A Phase 1 study of GDC-0134, a dual leucine
918 zipper kinase inhibitor, in ALS. Ann Clin Transl Neur *9*, 50–66. 10.1002/acn3.51491.

919 72. Chen, L., Nye, D.M., Stone, M.C., Weiner, A.T., Gheres, K.W., Xiong, X., Collins, C.A., and
920 Rolls, M.M. (2016). Mitochondria and Caspases Tune Nmnat-Mediated Stabilization to Promote
921 Axon Regeneration. Plos Genet *12*, e1006503. 10.1371/journal.pgen.1006503.

922 73. Kiryu-Seo, S., Tamada, H., Kato, Y., Yasuda, K., Ishihara, N., Nomura, M., Mihara, K., and
923 Kiyama, H. (2016). Mitochondrial fission is an acute and adaptive response in injured motor
924 neurons. Sci Rep-uk *6*, 28331. 10.1038/srep28331.

925 74. Rong, R., Xia, X., Peng, H., Li, H., You, M., Liang, Z., Yao, F., Yao, X., Xiong, K., Huang, J., et al.
926 (2020). Cdk5-mediated Drp1 phosphorylation drives mitochondrial defects and neuronal
927 apoptosis in radiation-induced optic neuropathy. Cell Death Dis *11*, 720. 10.1038/s41419-020-
928 02922-y.

929 75. Jahani-Asl, A., Huang, E., Irrcher, I., Rashidian, J., Ishihara, N., Lagace, D.C., Slack, R.S., and
930 Park, D.S. (2015). CDK5 phosphorylates DRP1 and drives mitochondrial defects in NMDA-
931 induced neuronal death. Hum Mol Genet *24*, 4573–4583. 10.1093/hmg/ddv188.

932 76. Chen, S., Liu, S., Wang, J., Wu, Q., Wang, A., Guan, H., Zhang, Q., Zhang, D., Wang, X., Song,
933 H., et al. (2020). TBK1-Mediated DRP1 Targeting Confers Nucleic Acid Sensing to Reprogram
934 Mitochondrial Dynamics and Physiology. Mol Cell *80*, 810-827.e7.
935 10.1016/j.molcel.2020.10.018.

936 77. Gan, X., Huang, S., Wu, L., Wang, Y., Hu, G., Li, G., Zhang, H., Yu, H., Swerdlow, R.H., Chen,
937 J.X., et al. (2014). Inhibition of ERK-DLP1 signaling and mitochondrial division alleviates
938 mitochondrial dysfunction in Alzheimer's disease cybrid cell. Biochimica Et Biophysica Acta Bba
939 - Mol Basis Dis *1842*, 220–231. 10.1016/j.bbadis.2013.11.009.

940 78. Yu, T., Jhun, B.S., and Yoon, Y. (2011). High-Glucose Stimulation Increases Reactive Oxygen
941 Species Production Through the Calcium and Mitogen-Activated Protein Kinase-Mediated
942 Activation of Mitochondrial Fission. Antioxid Redox Sign *14*, 425–437. 10.1089/ars.2010.3284.

943 79. Han, X.-J., Lu, Y.-F., Li, S.-A., Kaitsuka, T., Sato, Y., Tomizawa, K., Nairn, A.C., Takei, K., Matsui,
944 H., and Matsushita, M. (2008). CaM kinase Iα–induced phosphorylation of Drp1 regulates
945 mitochondrial morphology. J Cell Biology *182*, 573–585. 10.1083/jcb.200802164.

946 80. Yang, D., Rong, R., Yang, R., You, M., Wang, M., Li, H., and Ji, D. (2021). CaMK II -induced
947 Drp1 phosphorylation contributes to blue light-induced AIF-mediated necroptosis in retinal
948 R28 cells. Biochem Bioph Res Co *559*, 113–120. 10.1016/j.bbrc.2021.04.082.

949 81. Tedeschi, A., and Bradke, F. (2013). The DLK signalling pathway—a double-edged sword in
950 neural development and regeneration. Embo Rep *14*, 605–614. 10.1038/embor.2013.64.

951 82. Tortosa, E., Ghosh, A.S., Li, Q., Wong, W.R., Hinkle, T., Sandoval, W., Rose, C.M., and
952 Hoogenraad, C.C. (2022). Stress-induced vesicular assemblies of dual leucine zipper kinase are
953 signaling hubs involved in kinase activation and neurodegeneration. Embo J *41*, e110155.
954 10.15252/embj.2021110155.

955 83. Otera, H., Ishihara, N., and Mihara, K. (2013). New insights into the function and regulation
956 of mitochondrial fission. Biochimica Et Biophysica Acta Bba - Mol Cell Res *1833*, 1256–1268.
957 10.1016/j.bbamcr.2013.02.002.

958
959

Figure 1: Axotomy triggers a wave of DRP1-dependent mitochondrial fission, axon degeneration and cell death

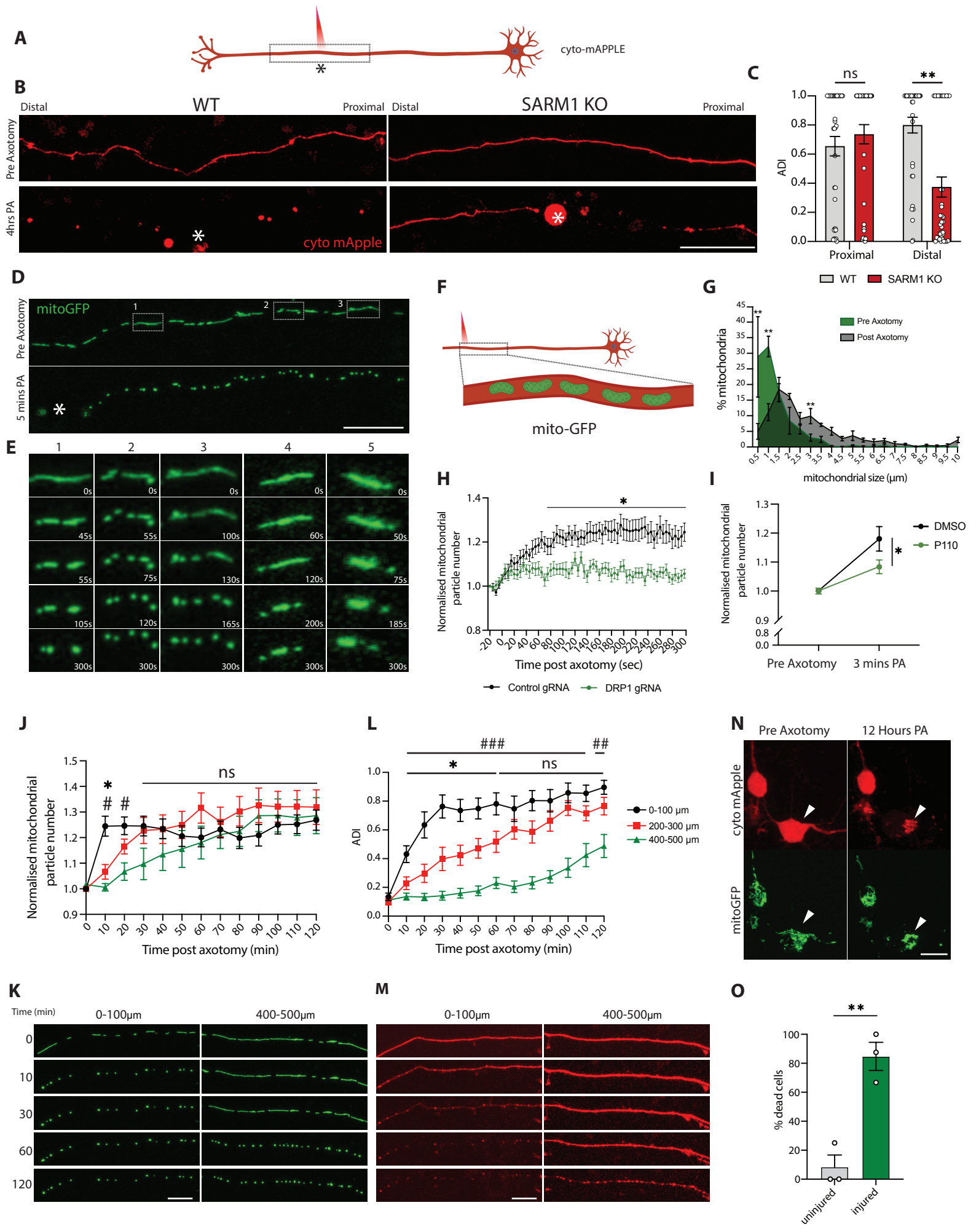

Figure 1 – Axotomy triggers a wave of DRP1-dependent mitochondrial fission, axon degeneration and cell death

A) Schematic representation of i3Neuron laser axotomy using Biorender. Dashed box indicates field of view. * Marks the site of axotomy
B) Representative images of WT and SARM1 KO axons transduced with cytoplasmic mApple (red) pre and 4 hours post axotomy (PA). * Marks the site of axotomy. (Scale bar = 100 µm).
C) Quantification of axon degeneration index (ADI) in WT and SARM1 KO neurons distal and proximal to the site of axon injury 4 hours post axotomy. Results are represented as mean ± SEM. N=3 independent differentiations, N≥ 38 axons. Two-way ANOVA, Bonferroni correction ($p \leq 0.01$ **, not significant, ns).
D) Representative images of i3Neuron axons transduced with mitoGFP (green) pre- and 5 minutes post axotomy (PA). * Marks the site of axotomy. (Scale bar = 20 µm). Time-lapse images of mitochondria shown in E.
E) Representative images of mitochondria undergoing fission after axon injury outlined in D.
F) Schematic representation of i3Neuron laser axotomy. Dashed box indicates field of view.
G) Quantification of mitochondrial length pre (green) and 5 minutes post axotomy (grey) (PA). Results are represented as mean ± SEM. N=3 independent differentiations, N≥ 28 axotomized neurons. Two-way ANOVA, Bonferroni correction ($p \leq 0.05$ *).
H) Normalized number of mitochondrial particles post axotomy in control and DRP1 KD neurons. Results are represented as mean ± SEM. N=3 independent differentiations, N≥ 25 axotomized neurons. Two-way ANOVA, Bonferroni correction ($p \leq 0.05$ *).
I) Normalized number of mitochondrial particles 3 mins post axotomy in DMSO and P110 treated neurons. Results are represented as mean ± SEM. N=3 independent differentiations, N≥ 26 axotomized neurons. Two-way ANOVA, Bonferroni correction ($p \leq 0.05$ *).
J) Quantification of axotomy-induced mitochondrial fission wave. Normalized number of mitochondrial particles post axotomy 0-100, 200-300 and 400-500 µm from the site of axotomy. Results are represented as mean ± SEM. N=3 independent differentiations, N≥ 23 axotomized neurons. One-way ANOVA, Bonferroni correction (*$p \leq 0.05$, 0-100 µm vs 200-300 µm, # $p \leq 0.05$, 0-100 µm vs 400-500 µm).
K) Representative images of axotomy-induced mitochondrial fission wave, Pre axotomy (0), 10-, 30- and 120-minutes post axotomy. Neurons sparsely transduced with mitoGFP (green). (Scale bar = 25 µm).
L) Quantification of axotomy-induced progressive axon degeneration. Axon degeneration index (ADI) 0-100, 200-300 and 400-500µm from the site of axotomy. Results are represented as mean ± SEM. N=3 independent differentiations, N≥ 14 axotomized neurons. (*$p \leq 0.05$, 0-100 µm vs 200-300 µm, ## $p \leq 0.01$, ### $p \leq 0.005$, 0-100 µm vs 400-500 µm).
M) Representative images of axotomy-induced axon degeneration. Pre axotomy (0), 10-, 30- and 120-minutes post axotomy. Neurons sparsely transduced with cyto-mApple (red). * Marks the site of axotomy. (Scale bar = 25 µm).
N) Representative images of axotomy-induced neuron death. Pre and 12-hours post axotomy. Arrow indicates axotomized neuron. Neurons sparsely transduced with cyto- mApple (red) and mitoGFP (green). (Scale bar = 40 µm).

1003 O) Quantification of axotomy-induced neuron death. Percentage of dead neurons 12 hours post
1004 axotomy. Results are represented as mean ± SEM. N=3 independent differentiations, N≥30
1005 axotomized neurons. Unpaired t-test ($p \leq 0.01$ **).

Figure 2: DLK regulates axotomy-induced mitochondrial fission

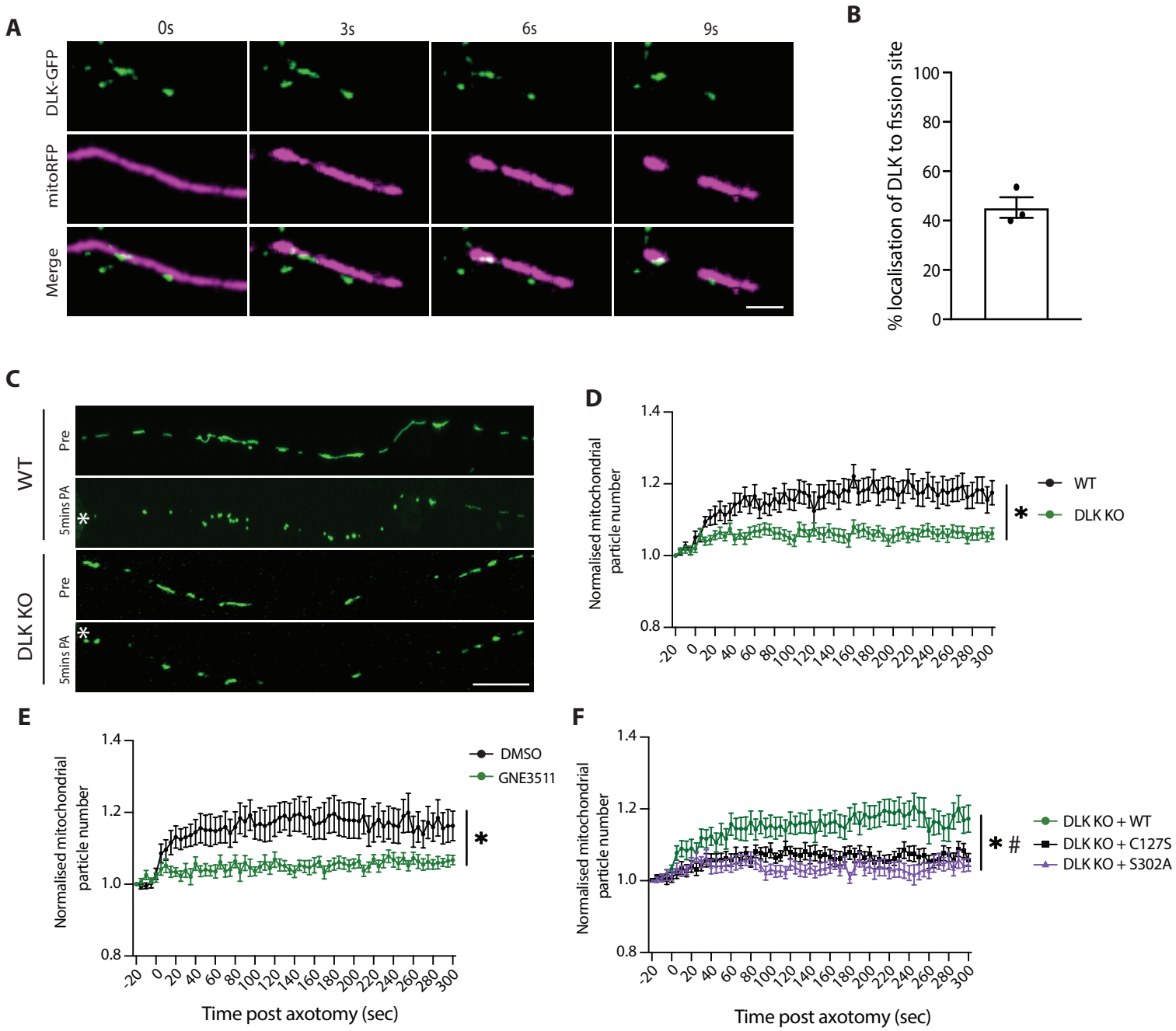

1006 **Figure 2 – DLK regulates axotomy-induced mitochondrial fission**
1007
1008 A) Representative images of DLK colocalization at the site of mitochondrial fission after
1009 axotomy. DLK-GFP (green) and mitochondria (mitoRFP, magenta). (Scale bar = 10 µm).
1010 B) Percentage mitochondrial fission events where DLK is localized at the site of fission. Results
1011 are represented as mean ± SEM. N=3 independent differentiations, N≥30 axotomized
1012 neurons.
1013 C) Representative images of WT and DLK KO neurons transduced with mitoGFP (green) pre (Pre)
1014 and 5 mins post axotomy (PA). * Marks the site of axotomy. (Scale bar = 25 µm).
1015 D) Normalized number of mitochondrial particles post axotomy in WT (black) and DLK KO (green)
1016 neurons. Results are represented as mean ± SEM. N=3 independent differentiations, N≥ 30
1017 axotomized neurons. (Two-way ANOVA, Bonferroni correction ($p \leq 0.05$ *)
1018 E) Normalized number of mitochondrial particles post axotomy in DMSO (black) and GNE3511
1019 (green)-treated neurons. Results are represented as mean ± SEM. N=3 independent
1020 differentiations, N≥ 25 axotomized neurons. (Two-way ANOVA, Bonferroni correction ($p \leq 0.05$
1021 *)
1022 F) Normalized number of mitochondrial particles post axotomy in DLK KO neurons transduced
1023 with WT DLK-GFP (green), DLK-C127S-GFP (black) or DLK-S302A-GFP (purple). Results are
1024 represented as mean ± SEM. N=3 independent differentiations, N≥ 23 axotomized neurons.
1025 Two-way ANOVA, Bonferroni correction (*$p \leq 0.05$, WT DLK vs DLK C127S, # $p \leq 0.05$, WT DLK vs
1026 S302A).

Figure 3: Activation of the DLK pathway by overexpression causes increased DRP1 phopshorylation

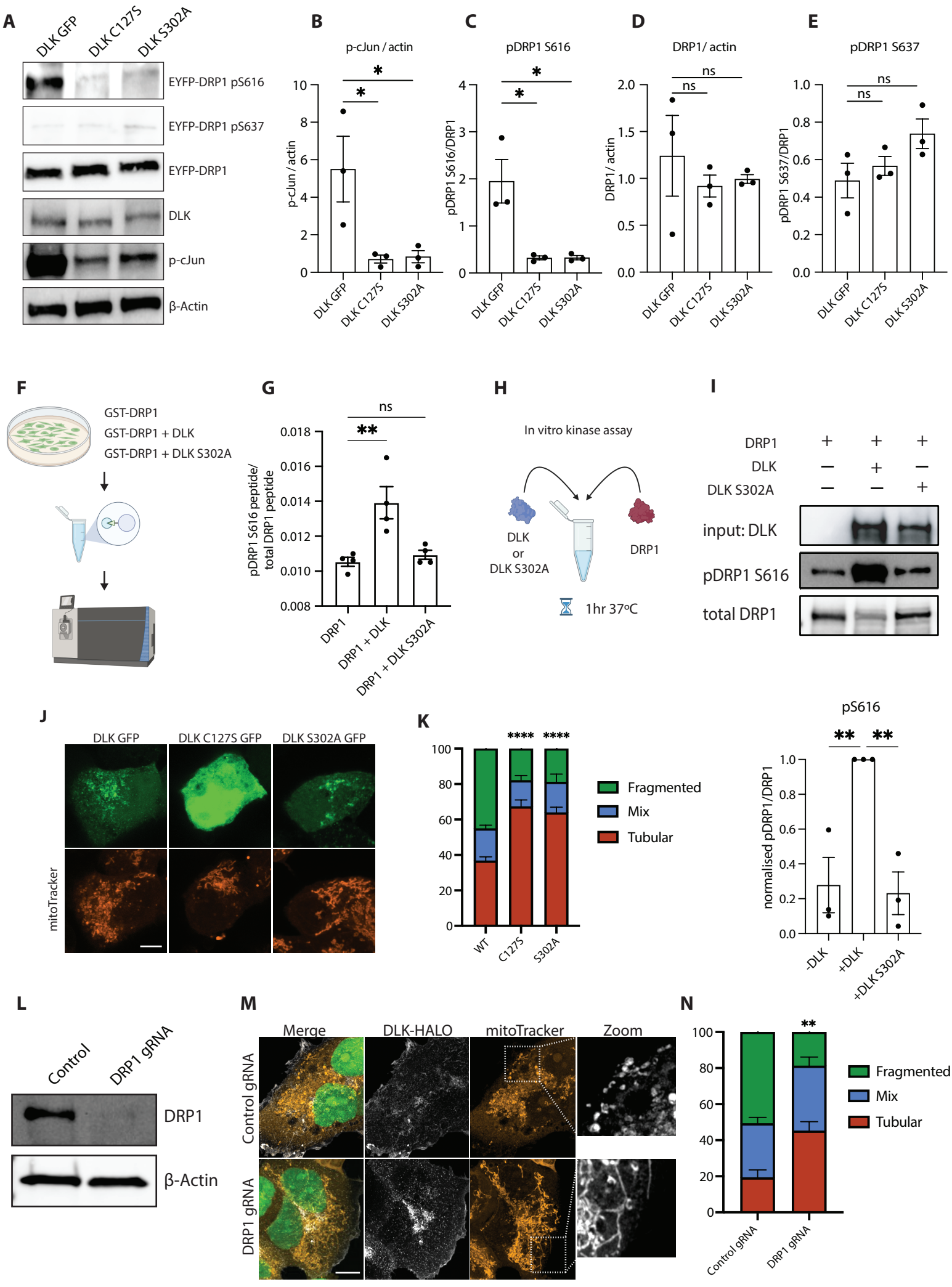

1027 **Figure 3 – Activation of the DLK pathway by overexpression causes increased DRP1**
1028 **phosphorylation**
1029
1030 A) Representative western blots of HEK293A cells transfected for 24 hours with WT, C127S and
1031 S302A DLK-GFP. Immunoblot for pS616-DRP1, pS637-DRP1, total DRP1, DLK, pS63-cJun and
1032 loading control ß actin.
1033 B) Quantification of pS63-cJun/ ß actin levels after 24-hour expression of WT, C127S and S302A
1034 DLK-GFP in HEK293A cells. Results are represented as mean ± SEM. One-way ANOVA,
1035 Bonferroni correction (p≤0.05 *).
1036 C) Quantification of pS616-DRP1/total DRP1 levels after 24-hour expression of WT, C127S and
1037 S302A DLK-GFP in HEK293A cells. Results are represented as mean ± SEM. One-way ANOVA,
1038 Bonferroni correction (p≤0.05 *).
1039 D) Quantification of total DRP1/ ß actin levels after 24-hour expression of WT, C127S and S302A
1040 DLK-GFP in HEK293A cells. Results are represented as mean ± SEM. One-way ANOVA,
1041 Bonferroni correction (not significant (ns)).
1042 E) Quantification of pS637 DRP1/ ß actin levels after 24-hour expression of WT, C127S and
1043 S302A DLK-GFP in HEK293A cells. Results are represented as mean ± SEM. One-way ANOVA,
1044 Bonferroni correction (not significant (ns)).
1045 F) Schematic representation of GST-DRP1 and DLK-GFP co-expression, purification and
1046 phospho-mass spectrometry.
1047 G) Phospho-mass spectrometry. pS616-DRP1 peptide / total DRP1 peptide levels from purified
1048 GST-DRP1 in HEK 293A cells expressing GST-DRP1, GST-DRP1 and DLK-GFP or GST-DRP1 and
1049 DLK-S302A-GFP. Results are represented as mean ± SEM. One-way ANOVA, Bonferroni
1050 correction (p≤0.01 **).
1051 H) Schematic representation of the *in vitro* kinase assay using purified DLK, DLK S302A and DRP1
1052 to test the direct phosphorylation of DRP1 by DLK.
1053 I) *In vitro* kinase assay. Utilizing separately purified DRP1, WT DLK and kinase dead DLK S302A.
1054 Representative immunoblots for pS616-DRP1, total DRP1 and DLK. Results are represented
1055 as mean ± SEM. One-way ANOVA, Bonferroni correction (p≤0.01 **).
1056 J) Representative images of HEK-293A cells expressing WT, C127S and S302A DLK-GFP (green)
1057 and mitoTracker (orange) for 24 hours. (Scale bar = 10 µm).
1058 K) Quantification of mitochondrial morphology in HEK293A cells transfected for 24 hours with
1059 WT, C127S and S302A DLK-GFP. N=3 individual transfections. Results are represented as
1060 mean ± SEM. Two-way ANOVA, Bonferroni correction (WT vs C127S p≤0.0001 ****, WT vs
1061 S302A p≤0.0001 ****, C127S vs S302A not significant ns).
1062 L) Representative western blots HEK-293A cells expressing dCAS9 transduced with control and
1063 DRP1 gRNAs. Immunoblot for total DRP1 and loading control ß actin.
1064 M) Representative images of Control and DRP1 KD HEK-293A cells expressing DLK-HALO for 24
1065 hours. NLS-GFP (green), DLK-HALO (white), mitoTracker (orange). (Scale bar = 10 µm).
1066 N) Quantification of Control and DRP1 KD HEK-293A cells mitochondrial morphology. Cells
1067 transfected for 24 hours with DLK-HALO. N=3 individual transfections. Results are
1068 represented as mean ± SEM. (Two-way ANOVA, Bonferroni correction (p≤0.01 **)
1069
1070

Figure 4: Axotomy causes DLK-dependent phosphorylation of DRP1

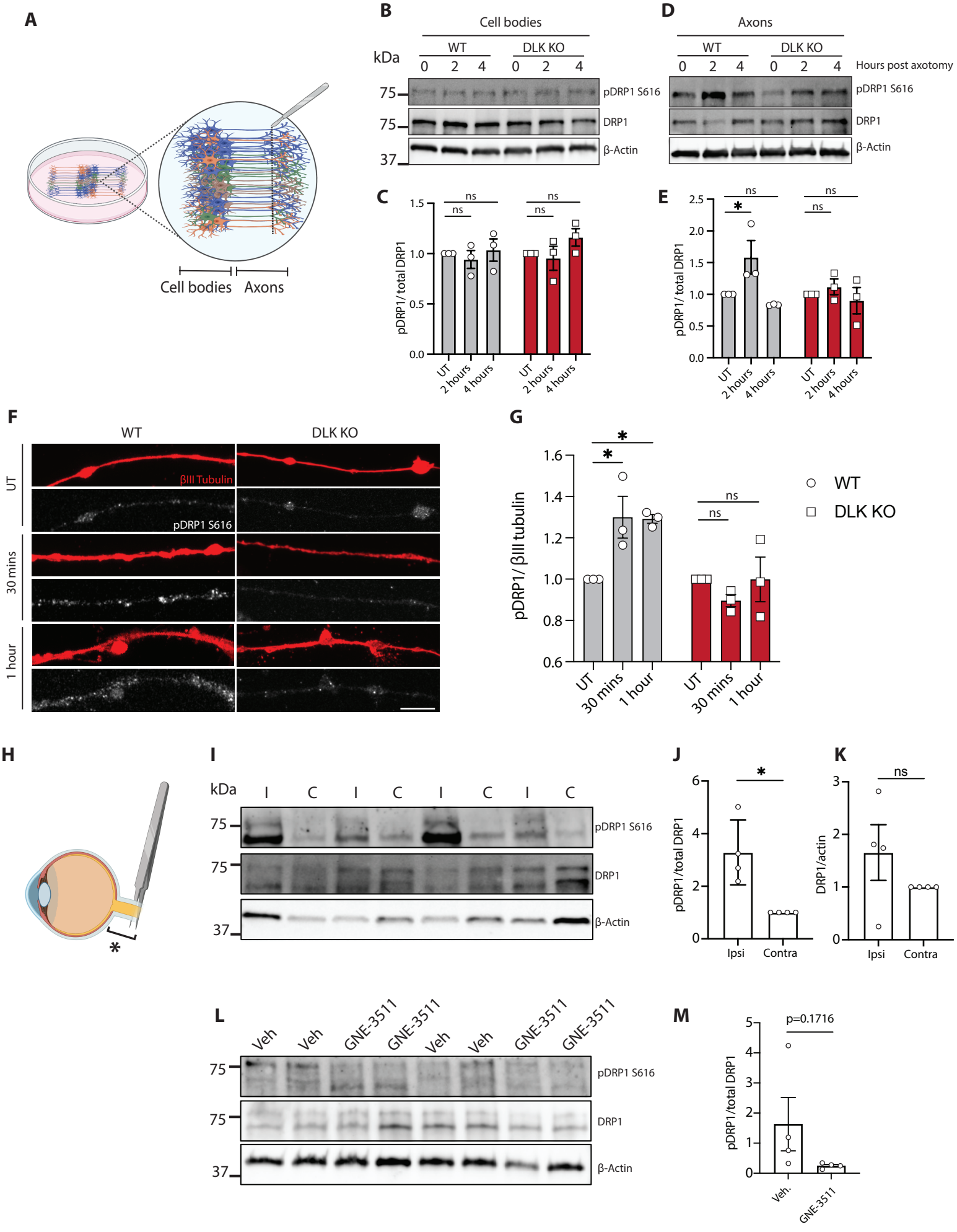

1071 **Figure 4 – Axotomy causes DLK-dependent phosphorylation of DRP1**
1072
1073 A) Schematic representation of i3Neuron center plating and axotomy for protein harvesting
1074 after injury.
1075 B) Representative western blots of WT and DLK KO neuron cell bodies untreated (UT), 2 and 4
1076 hours post axotomy. Immunoblot for p-S616 DRP1, total DRP1 and loading control ß actin.
1077 C) Quantification of pDRP1 (S616)/ total DRP1 levels in WT and DLK KO neuron cell bodies
1078 untreated (UT), 2 and 4 hours post axotomy. Results normalized to UT. Results are
1079 represented as mean ± SEM. N=3 independent differentiations. One-way ANOVA. No
1080 significant changes observed.
1081 D) Representative western blots of WT and DLK KO neuron axons untreated (UT), 2 and 4 hours
1082 post axotomy. Immunoblot for p-S616 DRP1, total DRP1 and loading control ß actin.
1083 E) Quantification of pDRP1 (S616)/ total DRP1 levels in WT and DLK KO neuron axons 0, 2 and 4
1084 hours post axotomy. Results normalized to UT. Results are represented as mean ± SEM. N=3
1085 independent differentiations. Two-way ANOVA. Bonferroni correction ($p \leq 0.05$*).
1086 F) Representative images of WT and DLK KO axons stained for ßIII tubulin (red) and pDRP1 S616
1087 (white) untreated (UT), 30 mins and 1 hour post axotomy. (Scale bar = 25 µm).
1088 G) Quantification of pDRP1 S616 fluorescence in WT and DLK KO neuron axons after axotomy.
1089 Results normalized to untreated axons. Results are represented as mean ± SEM. N=3
1090 independent differentiations. Two-way ANOVA, Bonferroni correction ($p \leq 0.05$ *)
1091 H) Schematic representation of optic nerve crush injury model. Bracket and * indicate the
1092 proximal portion of the injured nerve harvested for western blotting.
1093 I) Representative western blots of proximal portion of ipsilateral (I) injured and contralateral
1094 (C) optic nerves 24 hours after optic nerve crush. Immunoblot for p-S616 DRP1, total DRP1
1095 and loading control ß actin.
1096 J) Quantification of pDRP1 (S616)/ total DRP1 levels after optic nerve crush. Results normalized
1097 to contralateral side (C). Results are represented as mean ± SEM. Unpaired t-test ($p \leq 0.05$ *).
1098 K) Quantification of total DRP1/ ß actin levels after optic nerve crush. Results normalized to
1099 contralateral side (C). Results are represented as mean ± SEM. Unpaired t-test not significant
1100 (ns).
1101 L) Representative western blots of proximal portion of optic nerves 24 hours after optic nerve
1102 crush in mice treated with vehicle (veh) or DLK inhibitor (GNE-3511). Immunoblot for p-S616
1103 DRP1, total DRP1 and loading control ß actin.
1104 M) Quantification of total pDRP1 (S616)/ total DRP1 levels after optic nerve crush in mice treated
1105 with vehicle (veh) or DLK inhibitor (GNE-3511). Results are represented as mean ± SEM.

Figure 5: Inhibiting DRP1 delays axonal degeneration

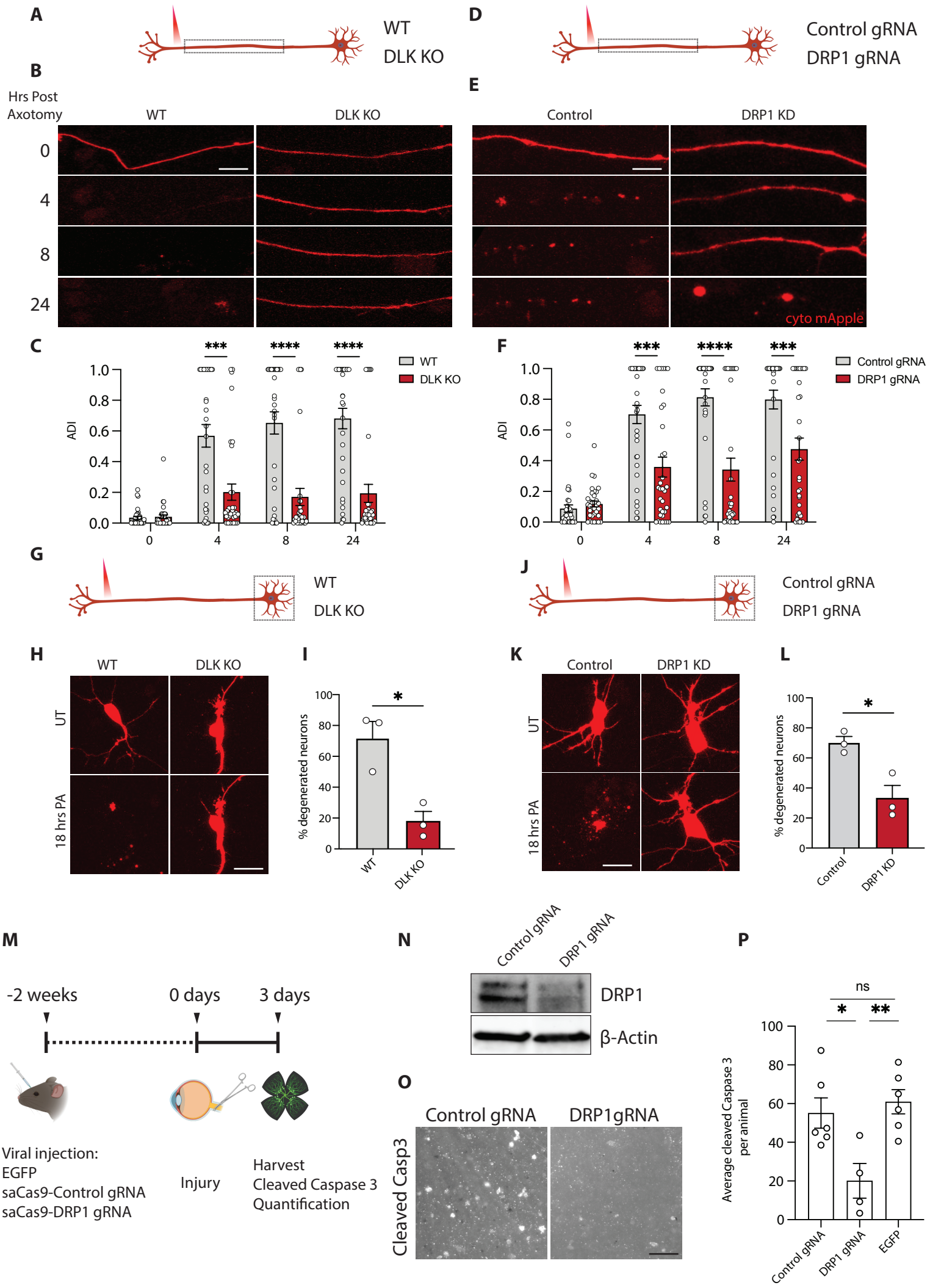

1106 **Figure 5 – Blocking DRP1 or DLK delays axon degeneration**
1107
1108 A) Schematic representation of i3Neuron laser axotomy. Dashed box indicates the field of view.
1109 B) Representative images of WT and DLK KO neuron axons transduced with cyto mApple (red)
1110 proximal to the site of injury 0,4, 8 and 24 hours post axotomy (Scale bar = 25 µm).
1111 C) Quantification of axon degeneration index (ADI) in WT and DLK KO neurons 0, 4, 8 and 24
1112 hours post axotomy. Results are represented as mean ± SEM. N=3 independent
1113 differentiations, N≥ 33 axons. Two-way ANOVA, Bonferroni correction (p≤0.005 ***, p≤0.001
1114 ****).
1115 D) Schematic representation of i3Neuron laser axotomy. Dashed box indicates field of view.
1116 E) Representative images of Control and DRP1 KD neuron axons transduced with cyto mApple
1117 (red) proximal to the site of injury 0, 4, 8 and 24 hours post axotomy (Scale bar = 25 µm).
1118 F) Quantification of axon degeneration index (ADI) in WT and DLK KO neurons 0, 4, 8 and 24
1119 hours post axotomy. Results are represented as mean ± SEM. N=3 independent
1120 differentiations, N≥ 33 axons. Two-way ANOVA, Bonferroni correction (p≤0.005 ***, p≤0.001
1121 ****).
1122 G) Schematic representation of i3Neuron laser axotomy. Dashed box indicates field of view.
1123 H) Representative images of WT and DLK KO neuron cell bodies transduced with cyto mApple
1124 (red) pre and 18 hours post axotomy (PA). (Scale bar = 40 µm).
1125 I) Percentage degenerated WT and DLK KO 18 post axotomy. Results are represented as mean
1126 ± SEM. N=3 independent differentiations. Unpaired t-test (p≤0.05 *).
1127 J) Schematic representation of i3Neuron laser axotomy. Dashed box indicates field of view.
1128 K) Representative images of Control and DRP1 KD neuron cell bodies transduced with cyto
1129 mApple (red) pre and 18 hours post axotomy (PA). (Scale bar = 40 µm).
1130 L) Percentage degenerated Control and DRP1 KD 18 post axotomy. Results are represented as
1131 mean ± SEM. N=3 independent differentiations. Unpaired t-test (p≤0.05 *).
1132 M) Schematic representation of RGC survival following optic nerve crush.
1133 N) Western blots of Control and DRP1 gRNA transduced optic nerved. Immunoblot for DRP1 and
1134 loading control ß actin.
1135 O) Representative images of cleaved caspase 3 positive cells in saCas9-Control and saCas9-DRP1
1136 gRNA transduced RGCs 3 days after ONC. (Scale bar = 25 µm).
1137 P) Average cleaved caspase 3 positive cells per animal in saCas9-Control, saCas9-DRP1 gRNA and
1138 EGFP transduced RGCs after nerve crush. Results are represented as mean ± SEM. N≥4
1139 animals per condition. One-way ANOVA, Bonferroni correction. (Control gRNA vs EGFP, not
1140 significant, ns. Control gRNA vs DRP1 gRNA p≤0.05 *. DRP1 gRNA vs EGFP p≤0.01 **).

Fig 6: BAX mediates cell death afer axotomy

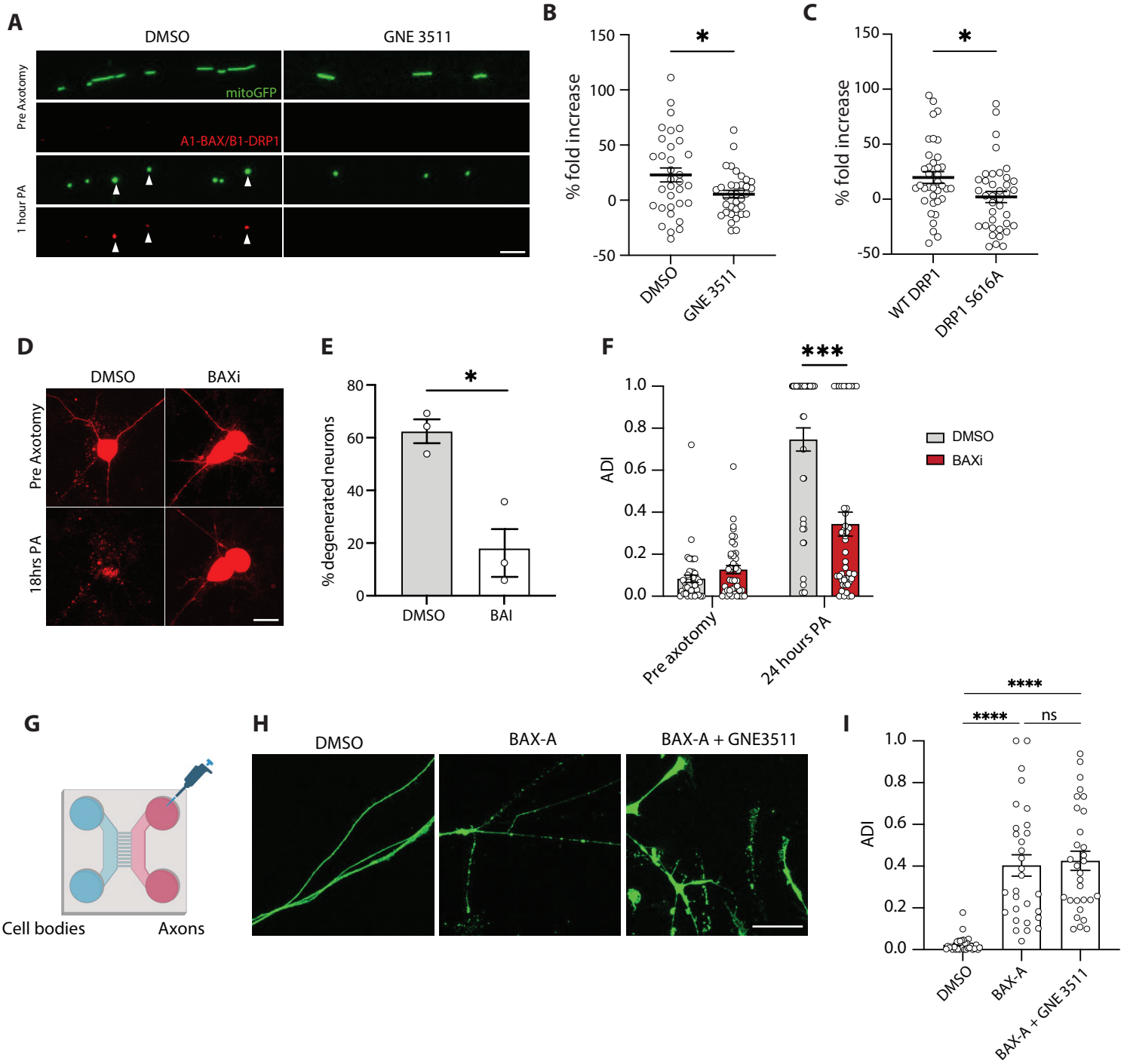

1141 **Figure 6 – BAX regulates cell death after axotomy**

1142

1143 A) Representative images of WT neurons treated with DMSO or GNE3511 pre- and 1-hour post-
1144 axotomy (PA) expressing mitoGFP (green) and A_1-BAX/B_1-DRP1 complexes (red). (Scale bar =
1145 5 µm).
1146 B) Quantification of A_1-BAX/B_1-DRP1 fluorescence fold change in the mitochondria of DMSO or
1147 GNE3511 treated neurons 1-hour post-axotomy. Results are represented as mean ± SEM. N=3
1148 independent differentiations, N≥ 34 axotomized neurons. Two-way ANOVA, Bonferroni
1149 correction. ($p \leq 0.05$ *).
1150 C) Quantification of A_1-BAX/B_1- WT DRP1 and A_1-BAX/B_1- DRP1 S616A fluorescence fold change
1151 in the mitochondria 1-hour post-axotomy. Results are represented as mean ± SEM. N=3
1152 independent differentiations, N≥ 34 axotomized neurons. Two-way ANOVA, Bonferroni
1153 correction. ($p \leq 0.05$ *).
1154 D) Representative images of DMSO and BAXi treated neuron cell bodies transduced with cyto
1155 mApple (red) pre and 18 hours post axotomy (PA). (Scale bar = 40 µm).
1156 E) Percent degenerated neurons 18 hours post axotomy treated with either DMSO or BAXi.
1157 Results are represented as mean ± SEM. N=3 independent differentiations. Unpaired t-test
1158 ($p \leq 0.05$ *).
1159 F) Quantification of axon degeneration index (ADI) of DMSO and BAX-A-treated neurons 24
1160 hours after axotomy. Results are represented as mean ± SEM. N=3 independent
1161 differentiations. One-way ANOVA, Bonferroni correction ($p \leq 0.001$ ***, not significant, ns).
1162 G) Illustration of microfluidic devices used to separate axons from somas allowing for the local
1163 treatment of i3Neuron axons.
1164 H) Representative images of WT axons separated using microfluidic chambers treated with
1165 DMSO, BAX-A or BAX-A + GNE3511 for 24 hours. (Scale bar = 25 µm).
1166 I) Quantification of axon degeneration index (ADI) of isolated axons treated with DMSO BAX-A
1167 and BAX-A + GNE3511 for 24 hours. Results are represented as mean ± SEM. N=3 independent
1168 differentiations. One-way ANOVA, Bonferroni correction ($p \leq 0.001$ ****, not significant, ns).